

Columbia Astrophysics Laboratory	XMM-RGS	Doc.: RGS-COL-CAL-98027 Page: 1 Auth.: Joshua Spodek Date: December 21, 1998
---	----------------	---

Review of the Physical Model Predictions with Comparison to the Panter Point Spread Function Measurements

Document title:	Review of the Physical Model Predictions
Document version:	1
Distribution:	
SRON:	T. den Boggende T. Bootsma A. Brinkman J.W. den Herder J. Kaastra R. Mewe F. Paerels C. de Vries
Columbia:	J. Cottam S. Kahn A. Rasmussen J. Spodek
LLNL:	T. Decker T. Dobson
PSI:	M. Guedel K. Thomsen
MSSL:	G. Branduardi-Raymont
ESTEC:	C. Erd F. Jansen G. Vacanti

1 Introduction

This memo documents the physical model of the XMM Reflection Grating Array (RGA) as it affects the point spread function (PSF) of the Reflection Grating Spectrometer (RGS). This memo also presents the comparisons between the model's predictions and the results of the PSF measurements of the RGS at Panter. These comparisons indicate how well the physical model approximates the true physical systems. Since the Panter tests were simple comparisons, they did not permit alterations to the physical model.

All of the input physical parameters to the model (with one exception, which is noted in section 4.1) were constrained by independent physical measurements prior to the Panter tests. Therefore none of these parameters were allowed to vary, which is why the comparisons between Panter data and simulated data are only comparisons, not fits. Although the simulation profiles are recentered and renormalized to reduce the χ^2 of the comparison, variation of these parameters does not affect the shape of the line profile.

The Panter campaigns are a test of our knowledge of the physical model of the RGS. This physical model is entirely determined by individual measurements made independently of the Panter tests, subject to the residual uncertainties of the independent measurements. The results of the Panter tests, when compared to the predictions made based on the physical model, lead to our understanding of the consistency of the physical model.

The structure of this memo is:

1. List of Panter measurements used in PSF determination and descriptions of their relevance to it
2. Description of the physical model, which is constrained entirely by measurements independent of the Panter campaigns
3. Review of all the results of the measurements
 - (a) August and December 1997 campaigns of RGS2/RGA1
 - (b) April 1998 campaign of RGS1/RGA2

This document does not present comparisons between physical model implementations, such as between the Columbia raytrace and Scisim. This comparison is underway, as proposed in [2].

A table of contents is at the end of the document.

2 List of Panter Measurements

Before the list of the measurements themselves is a list of the kinds of measurements that were used for PSF determination: focal searches, gluecksrads measurements, and full box measurements. This section describes the purpose of making a type of measurement and what information may be obtained from it, without reference to the actual measurement performed or particular considerations of a given measurement run. Later sections, which present the actual data, generally refer to specifics of a given measurement run without reference to why such a measurement was made.

2.1 Focal Searches

A focal search is a series of measurements at a set wavelength and order in which the RGS Focal-plane Camera (RFC) is placed at a range of intrafocal and extrafocal positions relative to the nominal Rowland circle. This type of measurement yields two types of information. First, the position of minimum spot width in the dispersion direction indicates the position of best focus. Second, the position of the cross-dispersion focus relative to the dispersion focus provides information on the location of the RGS with respect to the telescope focus, or alternatively, measures the defocusing of the RGA arraying. This second comparison works because the cross-dispersion position of best focus depends only on the telescope focal length, and is independent of the RGA alignment, whereas the dispersion position of best focus depends on the RGA alignment.

Determining RFC positions of best focus required modeling the spot width as a function of detector position. This model was not well determined and different models predicted different positions of best focus for the same set of data. Most models had broad minima, too, further decreasing the level to which the position of best focus could be constrained.

2.2 Gluecksrad

The gluecksrad (German for “Wheel of fortune”) is a mechanical device that restricts the light exiting the RGA to just that amount passing through an adjustable aperture. Figure 1 shows a map of the various apertures that may be opened in the device.

Information from gluecksrad measurements gives alignment information about the particular grating sectors whose light is passed by the open aperture. Since the gluecksrad is mostly circularly symmetric and the RGA is mostly rectangularly symmetric, there is always ambiguity as to which gratings or grating sectors misalignments should be ascribed when they are observed.

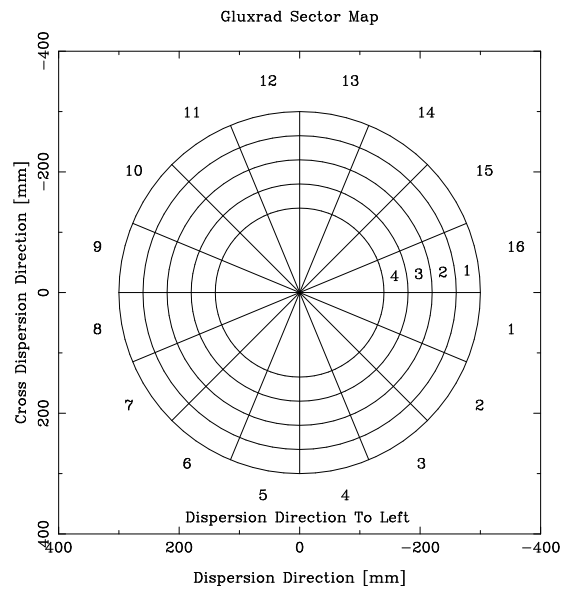


Figure 1: Gluecksrad sector map, viewed from upstream—that is, from the source. Photons are dispersed to the left, which is the spacecraft $-z$ direction. The spacecraft $+y$ direction is up, and the $+x$ direction is into the page.

Because of the small apertures and correspondingly small count rates, no gluecksrad measurement provided reliably quantifiable information beyond the first moment of the distribution—that is, the position of the spot center. On the other hand, since no hardware was moved between gluecksrad measurements in a given series of runs, comparisons of spot centers between data and simulation were valid across the entire series, not just a single measurement. This correspondence between individual gluecksrad measurements allowed tighter constraints on the data, since recentering of data and simulation spots could only be done for entire runs, not individual spots.

Columbia Astrophysics Laboratory	XMM-RGS	Doc.: RGS-COL-CAL-98027 Page: 4 Auth.: Joshua Spodek Date: December 21, 1998
---	----------------	---

For example, figures 2 show two pairs of spot profile comparisons indicating the level of correspondence possible between data and simulation. Recentring the bottom two peaks in figure 2 would decenter those in the top two plots. as well as all the other unshown peaks from the same gluecksrad run. Thus, taking more gluecksrad measurements did not increase the number of physical parameters.

Also observable by eye, though not reliably quantifiable due to the low gluecksrad count rates, was the general consistency in the profile morphologies between simulated and real gluecksrad data. This consistency can be seen in the top two and bottom right profiles in figure 2. That the profile shape was consistent even when displaced, as in the bottom right plot, suggested that the displacement was due to a coherent grating misalignment. This coherence suggests that the misalignment was not due to environmental testing or RGA transportation, both of which would tend to randomize grating misalignments.

The degree of coherence in grating misalignments is poorly quantified and is therefore this coherence only suggestive. Since profile morphologies are also to a large extent due to the position on the RGA of the gluecksrad aperture, other effects may, at least, partially explain the consistency.

Figure 3 compares the two-dimensional appearance of data and simulated spots. The scales of the data and simulation plots are not equal and, as shown, allow no quantitative comparison. Nonetheless, qualitative comparison of morphologies are valid and often useful as simple checks. The non-circular morphologies exhibited in figure 3 are the expected behavior of the ideal RGS when vignettted by a gluecksrad type obscuration. The shapes seen are largely determined by the position on the RGA of the gluecksrad aperture and familiar properties of the Wolter geometry of the telescope.

Gluecksrad measurements were performed in:

- Al K, m=-1 (RGS2/RGA1)
- Mg K, m=0 (RGS1/RGA2)

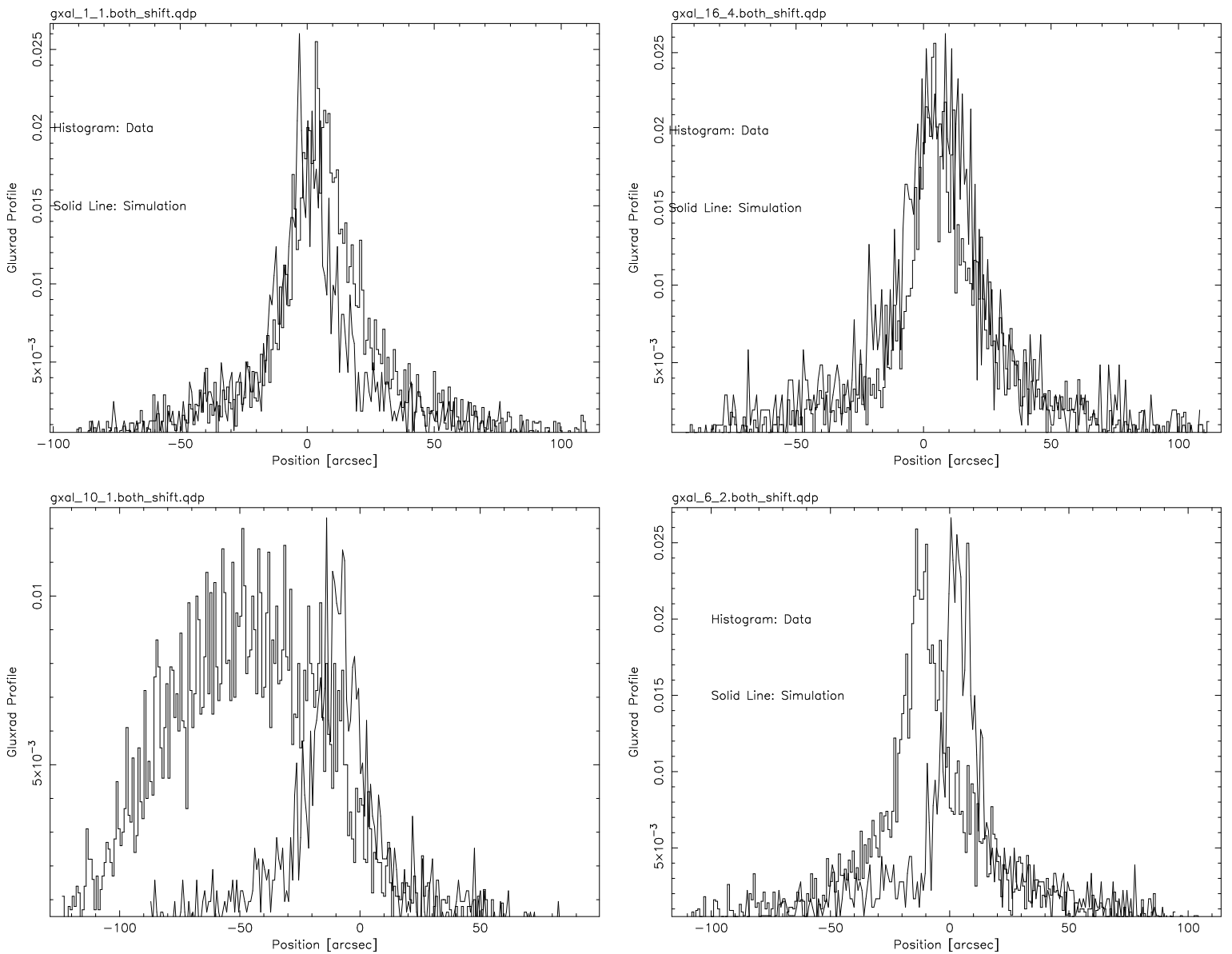
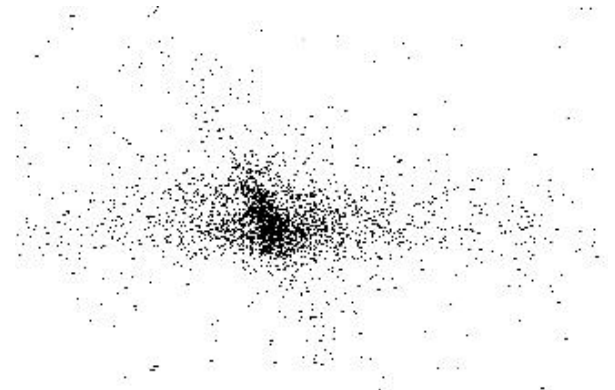
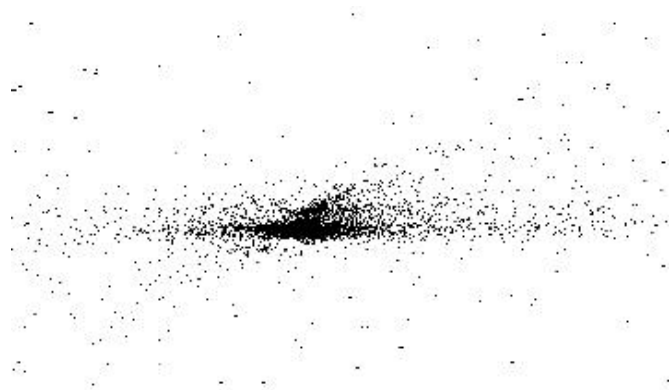
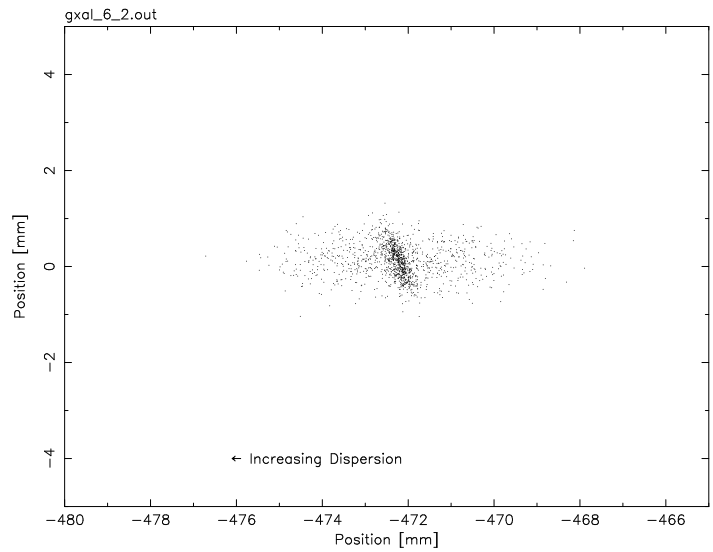
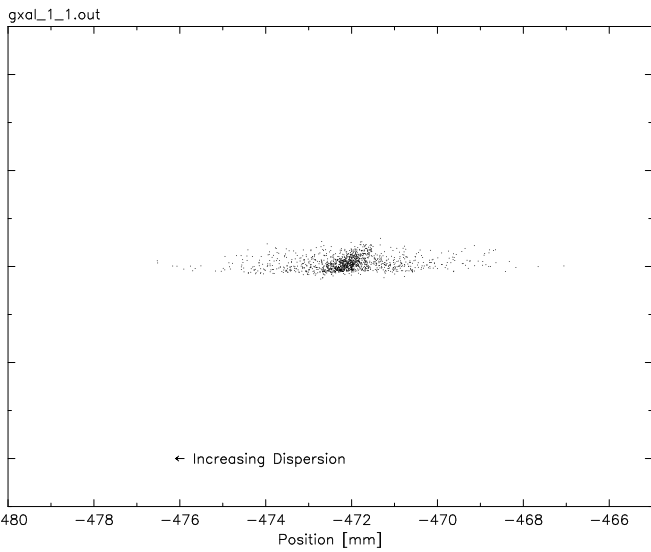


Figure 2: Spot profiles of four gluecksrad sectors. Not enough counts were taken to quantify higher order moments than centers in these or any other gluecksrad measurements, but general morphologies are readily observed. Top two: data and simulation profiles were consistent in positions of centers and general shape. Bottom left: this sector contained gratings whose misalignment in the RGA was apparent to the unaided eye. Bottom right: the misalignment of the gratings in this sector was more subtle. That the morphology is similar in real and simulated data suggests a coherent misalignment, probably not resulting from environmental testing.



Gluxrad Simulation Result

Gluxrad Simulation Result



spodek 25-Oct-1997 16:45

spodek 25-Oct-1997 16:46

Figure 3: Scatter plots of data from gluecksrads measurements of two sectors from well separated apertures. The spot morphologies are largely dictated by the location on the RGA of the glueckrad sector. Top: actual data; bottom: simulated data.

Columbia Astrophysics Laboratory	XMM-RGS	Doc.: RGS-COL-CAL-98027 Page: 7 Auth.: Joshua Spodek Date: December 21, 1998
---	----------------	---

2.3 Full Box

Examples of full box results may be seen in section 4.

The full box PSF measurements provide an overall assessment of the RGS at a particular wavelength and order. The choice of line energy for PSF full box measurements was determined by the desire for narrow lines and a large range in exit graze angle, β . Narrow lines are desirable in order that the intrinsic line width contribute minimally to the observed line width. A range in β is important since it is a critical parameter upon which the angular profile of scattered light depends. High scatter is desirable diagnostically, in order to maximize the effect of the scattering properties of the gratings.

In general, narrow lines with high scatter are high orders of high energy lines. Narrow lines of lower energy than the chosen Si, Al, and Mg K lines could not easily be produced in the laboratory. Moreover, in order to achieve high β 's with lines of low wavelength, high diffraction orders were used. Often the lines used, particularly at high orders, are not within the useful range for astronomical observations, even though they provide more constraining data for our present purposes. It should be kept in mind that the criteria for choice of lines at Panter is based on diagnostic power of the lines.

The superficial appearance of high order, high energy, high scatter lines is that of a very broadened line. This appearance is exacerbated by the display of the data on plots with logarithmic vertical axes, which further accents the scattering wings, again increasing their diagnostic power. The reader should not be discouraged by this superficial appearance: despite their utility for the task at hand, these lines are not the best tools for direct assessment of the RGS's true resolution at astronomically interesting energies or orders.

The lines ultimately used were:

- Si K, $m=0,\dots,-4$
- Al K, $m=0,\dots,-4$
- Mg K, $m=0,\dots,-4$
- O K, $m=0,\dots,-2$ (monochromator)

The data from comparisons with Panter Si and O data was less constraining than Al and Mg data for PSF measurements. The Si K line, it turns out, has satellite structure whose properties are not constrained by independent measurement, and therefore were poorly simulated. The O line was broad compared to the broadening caused by RGS misalignments. Panter's monochromator was used to narrow the line, but introduced new uncertainties that could not be well modeled.

Table 1 shows various parameters of the lines used for PSF measurements (plus Cu L), including information on the lines' centers, satellite structure, exit angles for on axis illumination, and predicted fraction of scattered light. β_m indicates the exit angle for order m and TIS_m (for total integrated scatter) indicates the fraction of light scattered from the line's core at order m .

For RGS2/RGA1, full box data from two configurations were used. Configuration A denotes the nominal configuration. Configuration B0 denotes the configuration where the RGA was moved toward

Columbia Astrophysics Laboratory	XMM-RGS	Doc.: RGS-COL-CAL-98027 Page: 8 Auth.: Joshua Spodek Date: December 21, 1998
---	----------------	---

Name	E(keV)	$\lambda(\text{\AA})$	(Width) $\Delta\lambda(\text{\AA})$	(Satellite) $\lambda(\text{\AA})$	β_{-1}	β_{-2}	β_{-3}	β_{-4}	TIS_{-1}	TIS_{-2}	TIS_{-3}	TIS_{-4}
Si K	1.74	7.126	4.8E-3	6.77	2.35	2.92	3.40	3.82	0.648	0.709	0.753	0.786
Al K	1.486	8.344	4.8E-3	8.29	2.45	3.09	3.62	4.08	0.590	0.656	0.703	0.740
Mg K	1.25	9.89	9.5E-3	9.82	2.58	3.30	3.88	4.39	0.530	0.599	0.649	0.689
Cu L	0.929	13.34	0.03	N/A	2.85	3.71	N/A	N/A	0.435	0.505	N/A	N/A
O K	0.525	23.62	4.0E-4	N/A	3.54	4.75	N/A	N/A	0.295	0.359	N/A	N/A

Table 1: Parameters of the lines used for PSF measurements at Panter

the mirror module by 6.0 mm, which is the flight configuration for RGS2/RGA1. This document does not present data from measurements taken in the configuration where the RGA was both translated and rotated.

The plots shown in section 4 show a χ^2 value for each plot. This χ^2 value is determined in the usual way, but is minimized only by choosing the smallest value over a grid of point in the parameter space of spot position, Δx , and number of counts, ΔN_{counts} . Since only these parameters do not in any way affect the profile shape, and are not a part of the physical model, they are allowed to vary. Since changes in Δx have a non-analytic, discrete effect on χ^2 between two sets of binned data, traditional minimization routines don't work. For this reason χ^2 is chosen from the grid of points in parameter space.

2.4 Detailed list of Measurements performed

Tables 2–4 list the various measurements performed at Panter, including both PSF related and non-PSF related measurements. Some references are also given to other documents that report on results based on those measurements.

Columbia Astrophysics Laboratory	XMM-RGS	Doc.: RGS-COL-CAL-98027 Page: 9 Auth.: Joshua Spodek Date: December 21, 1998
---	----------------	---

Measurement Type	Source	$\lambda(\text{\AA})$	Order	Obs	Session	Where to find results
Focus Search	Al	8.314	-1	18	7-12	COL-CAL-97018
				19	2-5	
	Mg	9.89	0,-1,-3,EPIC	38	6-21	
			-3	55	17-20	
Effective Area	Si	7.126	-4-0	31	2-16	SRON-TN-CAL97003
			-3-0,EPIC	49	4-13	
	O	23.6	-2-0	31	1-8	
			-2-0	49	14-19	
	Fe		-2-0	33	3-10	
			-2-0	52	1-7	
	Cu	13.34	-4-0	34	1-9	
			-4-0	43	2-7	
	P		-3-0,EPIC	34	13-19	
				35	1-8	
			-2-0,EPIC	59	1-5	
	Al	8.314	-3-0	55	4-9	
	Mg	9.89	-3-0,EPIC	55	10-26	
	Ti		-2-0,EPIC	58	4-8	
Mo		-2-0,EPIC	58	9-14		
C		-2-0,EPIC	60	4-8		
Co		-2-0,EPIC	64	2-7		
Cr		-2-0,EPIC	64	11-16		
Point Spread Function	Al	8.314	-2,0,EPIC	16	5-7	COL-CAL-97018 and COL-CAL-97024 (see COL-CAL-97020 for FM1B predictions based on FM1 data)
			18	4,5		
	Mg	9.89	-4-0,EPIC	24	1-9	
			-3-0	32	11-20	
			-4,-2	39	1-9	
			-2	40	2	
		-3,EPIC	41	14-16		
O	23.6	-2-0	26	2-4		
		-2-0	44	4-8		
Si	7.126	-3-0,EPIC	26	5-9		
		-5-0	39	10-16		
		-4-0	44	9		
			46	1-14		
Off-Axis	Al	8.314	-3(-6' < ϕ < 2')	40	3-7	SRON-TN-CAL97003
			-2,-1(-21' < ϕ < 21')	60	9-25	
		61	3-6			
	Mg	9.89	-2-0(-21' < ϕ < 21')	40	9-14	
			41	1-12		
Cu	13.34	-2(-4' < ϕ < 2')	41	17-20		
Ti		-1(-8' < ϕ < 2')	47	2-16		
Gluecksrad	Al	8.314	-1	20	8-28	COL-CAL-97018 and COL-CAL-97024
				21	4-15	
				47	11-20	
Mg	9.89	-3	55	22-26		
Si	7.126	-3,0,EPIC	59	6-10		
Continuum	Cu			64	8	
				64	10	

Table 2: List of measurements performed on RGS2/RGA1 in the August 1997 Panter run.

Columbia Astrophysics Laboratory	XMM-RGS	Doc.: RGS-COL-CAL-98027 Page: 10 Auth.: Joshua Spodek Date: December 21, 1998
---	----------------	--

Measurement Type	Source	$\lambda(\text{\AA})$	Order	Obs	Session	Where to find results
Focus Search	Mg	9.89	EPIC	16	6-15	COL-CAL-97022
			-3	16	16-27	
			0	16	28-36	
				17	2-3	
			-1	17	5-9	
		18	3-6			
		18	7-17			
	Al	8.314	-1	19	10-21	
			-4	20	5-13	
			EPIC	33	4-12	
0	21.0	-1	20	16-23		
		EPIC	21	3-11		
		EPIC	28	16-22		
Effective Area	O	21.0	-1,0,EPIC	23	4-8	SRON-TN-CAL-98001
			-1,0,EPIC	23	9-14	
			-1,-2	25	2-7	
			-1,0,EPIC	25	8-10	
			-1,EPIC	25	11,12	
			-2-0,EPIC	26	6-12	
	Cu		-2-0,EPIC	27	3-7	
	Al	8.314	-2-0,EPIC	27	9-13	
	Mg	9.89	-3-0,EPIC	28	2-7	
	Si	7.126	-3-0,EPIC	28	8-14	
	O	23.6	-1,0,EPIC	32	4-7	
	Fe		-2-0,EPIC	32	9-14	
	C		-1,0,EPIC	32	16-22	
Point Spread Function	Mg	9.89	-3-0,EPIC	18	18-25	COL-CAL-97022
				19	3-9	
	O	21.0	-1	21	2	
			-1,0	21	12-15	
		-2	26	2-5		
C		EPIC	33	3		
Off-Axis	Al	8.314	$(-21' < \phi < 21')$	34	3-10	SRON-TN-CAL-98003
Continuum	Au			33	13-23	

Table 3: List of measurements performed on RGS2/RGA1 in the December 1997 Panter run.

Columbia Astrophysics Laboratory	XMM-RGS	Doc.: RGS-COL-CAL-98027 Page: 11 Auth.: Joshua Spodek Date: December 21, 1998
---	----------------	--

Measurement Type	Source	$\lambda(\text{\AA})$	Order	Obs	Session	Where to find results	
Focus Search	Mg	9.89	0,EPIC	7	10-38	COL-CAL-98006	
			-2,-4	8	2-24		
			EPIC	13	2-12		
	O	24.0	-1,EPIC	18	15-37		
			0	21	6-16		
		23.6	-2	22	11-24		
Effective Area	Mg	9.89	-3-0	12	19-22		
	Cu	13.34	-2-0	13	24-27		
	Al	8.34	-4-0	14	1-5		
	O	23.6	0	14	10		
			-1,-2	15	2,3		
			-1,0,EPIC	22	4-9		
			0,-1	23	2-7		
			21.0	-2-0	28		3-9
			30.0	0,-1	23		2-7
			18.0	-2-0	28		3-9
		24.0	-1,0	20	1-4		
Fe		-2-0	15	10-13			
Si	7.126	-5-0	16	3-7			
C		-1,0	18	2-6			
Point Spread Function	Mg	9.89	-2	8	26	COL-CAL-98006 and COL-CAL-98013	
			-3,-1,0,EPIC	9	2-17		
			0	33	33		
			-3,EPIC	34	4,3		
	O	24.0	-1	18	39		
			0	21	17		
			-2	22	25		
			-2-0	31	4-7		
		0,EPIC	34	8,7			
Si	7.126	-1	34	9			
Off-Axis	Al	8.34	$(-21' < \phi < 14')$	37	6-20		
			$(-14' < \phi < 14')$	41	3-13		
Gluecksrad	Mg	9.89	0	10	7-16	COL-CAL-98006 and COL-CAL-98013	
				11	1-22		
			0,EPIC	33	6-30		
Continuum	Au			16	8-10	(in preparation: check web page soon)	
				17	1		
	SiO ₂		34	11			
	C		38	3			
	MACOR			39	3		

Table 4: List of measurements performed on RGS1/RGA2 in the April 1998 Panter run.

3 Description of the Physical Model: What we know and how we know it

This section presents the values for the physical parameters that affected our predictions of the PSF. The parameters are presented by the physical component or process to which they relate:

- Line Profile
 - Core Wavelength
 - Satellite Wavelength
 - Satellite Normalization
- Telescope Model
- Measurement Geometry
 - Apparatus position uncertainties
 - Apparatus position reproducibility
 - Spot position reproducibility
- Mechanical Tolerancing on Grating Positions
 - Assembly Room Data
 - Machining Specifications
- Scattering Model
 - Small Angle Scattering Only
 - Fermi-Dirac form
 - σ, l from Nevis and EQM deep exposures

The parameters to be presented are constrained by independent, prior measurement, but are also those that produce the best consistency with the Panter data. Extensive sampling of most parameters has been performed, but no alterations have produced a uniform improvement in all comparisons. Moreover, any alternate parameter sets require deviations of the model from the externally measured input values.

3.1 Line Profiles

Each line—Si K, Al K, Mg K, and O K—was chosen for its properties of being narrow, high energy, and therefore highly scattering. As it turns out, each line has its own characteristics that alter it from being ideal. These characteristics must all be accounted for in the physical model in order that departures from the ideal in the RGS can be ruled out when Panter observations reveal imperfections.

Columbia Astrophysics Laboratory	XMM-RGS	Doc.: RGS-COL-CAL-98027 Page: 13 Auth.: Joshua Spodek Date: December 21, 1998
---	----------------	--

3.1.1 General

Al K and Mg K both have well-known satellite lines. Their intrinsic widths are small compared to the contributions to the observed widths due to departures from the ideal RGS, but these intrinsic widths start to become resolvable in higher orders and therefore must be taken into account. Si K appears to have satellite structure, but is not well known enough to constrain its properties. O K's intrinsic width is large relative to the contributions to the observed line widths due to departures from the ideal RGS at all orders, so it must always be taken into account. The use of the Panter monochromator requires a monochromator model, which cannot be well constrained by prior knowledge.

3.1.2 Core Wavelengths

The core wavelengths of all our lines are well known.

3.1.3 Core Widths

The core widths are well known for isolated atoms, but must be modified when the source is in a solid state environment. Line widths for Al K and Mg K were obtained from [1]. No similar information could be found for Si K, so lacking prior measurement, the width of Si K was arbitrarily set to that of Al K. No changes were made to the Si K width.

The O K line width was given by a simple model of the Panter monochromator. The monochromator, which physically consists of a rotatable grating which conically diffracts light toward an adjustable slit, has evidently been fraught with operational difficulties. The simple model, due to Frits Paerls, used in the present physical model assumes light from the grating uniformly fills the slit, which cuts the light off with a step function at its boundaries. Thus the input profile of the O K line is flat, with a width determined by

$$\frac{\lambda}{\Delta\lambda} = 800, \quad (1)$$

where the 800 is determined by the slit's physical width. Owing to this large width, the O data was of less diagnostic value than other lines.

It has been suggested that the shorter source distance arising from the monochromator's added reflection could affect the O K data by changing the position of best focus. It was not possible to determine whether or not this effect had observable consequences in the O K data.

3.1.4 Satellite separations and relative intensities

The Mg K and Al K lines have well-known satellite structure. The satellite lines have been measured by AXAF's Low Energy Transmission Grating Spectrometer in eighth order during its testing phase. The Mg K line was also measured in second order by the RGS during its Electro-Optical BreadBoard (EOBB) test phase. The EOBB testing included a second order illumination of a single, relatively flat grating.

Columbia Astrophysics Laboratory	XMM-RGS	Doc.: RGS-COL-CAL-98027 Page: 14 Auth.: Joshua Spodek Date: December 21, 1998
---	----------------	--

The RGS data is available in [3], figure 10b. The AXAF data is available in [4], figures 7a (Al), 7c (Al), and 11 (Mg). In the case of Mg, values were averaged between those found from RGS and AXAF data. Unfortunately, digital images of the plots remain unavailable for inclusion here.

Satellite structure was observed in first order Si data. No published data was available on this structure. Since the observed satellite structure was well removed from the core in first order and completely unobserved in second order, an empirical fit was made, using RGS data. The resulting simulation core was essentially unchanged.

The values ultimately used are:

Source Name	Core Wavelength	Core Width	Satellite Wavelength	Satellite Width	Relative Intensity
Mg	9.890 Å	9.000×10^{-3} Å	9.820 Å	15.0×10^{-3} Å	85:15
Al	8.344	4.773×10^{-3}	8.294	4.773×10^{-3}	90:10
Si	7.126	4.773×10^{-3}	6.770	50.0×10^{-3}	90:10

Table 5: Satellite line parameters for Al and Mg.

3.2 Telescope Model

At the time of testing, no explicit model for the FM3 mirror module was available, so a simplified, idealized model was the only choice. The telescope model of the physical model was relatively close to the ideal model, with simple, empirical parametrizations of the deviations from ideal seen in the EPIC data.

Once the parameters were fixed by the EPIC data they were unchanged in the RGS PSF data.

The same physical telescope, FM3, was used in all Panter RGA measurements.

The physical model started with the nominal A, B, C, D, and E coefficients that described the ideal mirror shells. To these shells were added a Lorentzian distribution of surface normal perturbations with a width of 3.97 arcseconds. Additionally, a Gaussian distribution of shell centers with a width of 60 μm was added to simulate the non-coincidence of the 58 optical axes.

Figures 4–5 show comparisons between EPIC data from Panter non-PSF data and simulated telescope spots over a range of line energies. In principle the telescope model should have only very weak dependence on source energy. We expect some degradation in the comparison at O K from the inadequacies of the monochromator modeling.

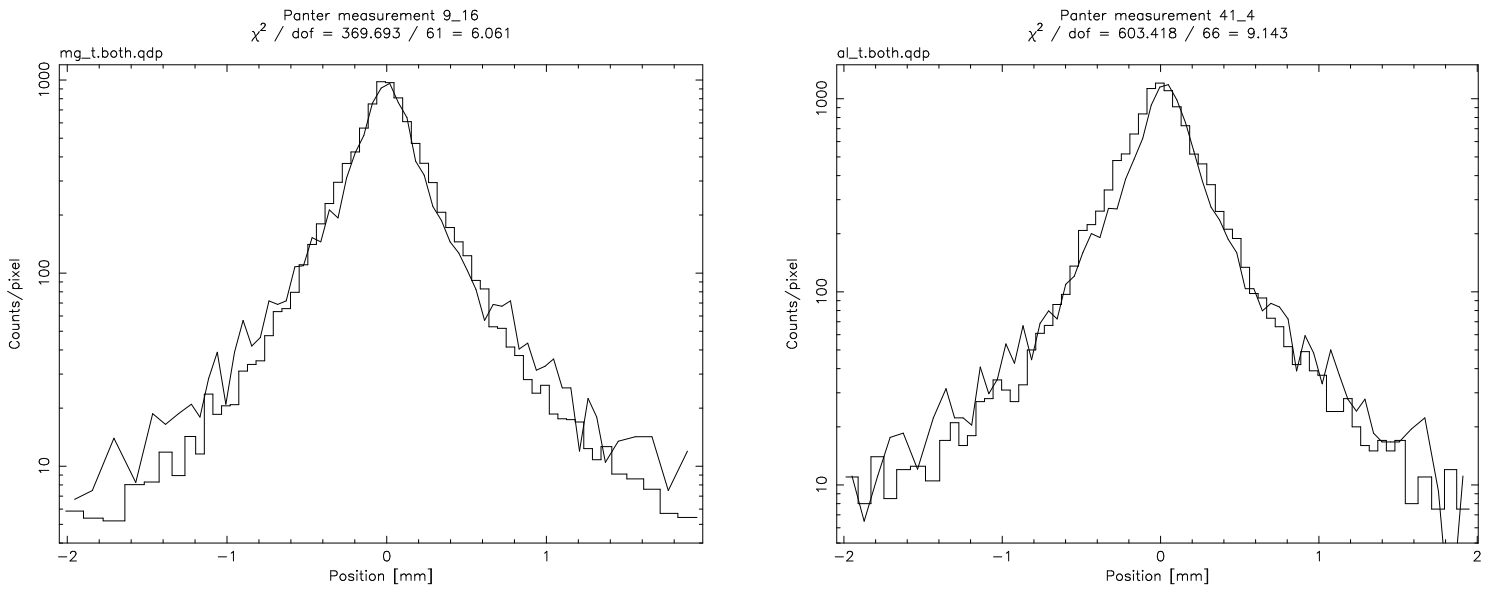


Figure 4: EPIC telescope Panter data and simulated data for Mg (left) and Al (right).

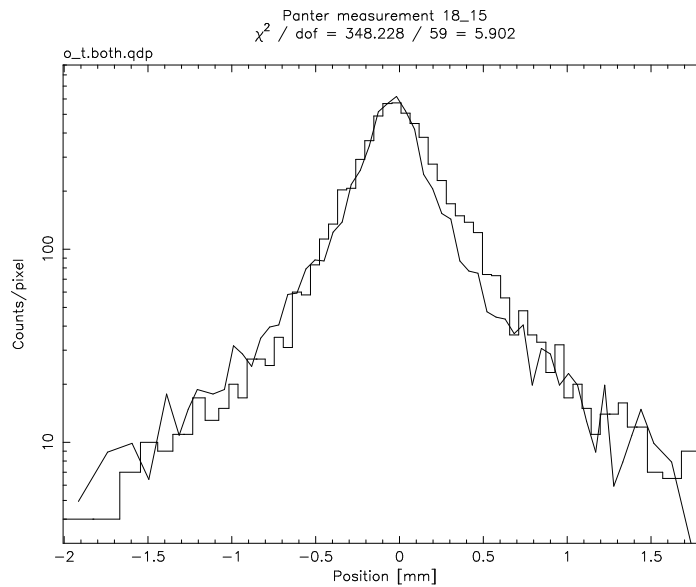


Figure 5: EPIC telescope Panter data and simulated data for O, incorporating the telescope model as described in this section, as well as the monochromator model described above.

Columbia Astrophysics Laboratory	XMM-RGS	Doc.: RGS-COL-CAL-98027 Page: 16 Auth.: Joshua Spodek Date: December 21, 1998
---	----------------	--

3.3 Measurement Geometry

A detailed report of the results presented in this section is available in [5].

3.3.1 Apparatus position uncertainties

The positions of all the optical apparatus used in the measurement must be accurately known in order to simulate the measurement as actually performed. All hardware positions in the simulations come from the hardware positions reported by the Panter measurement devices, principally the theodolite.

The theodolite measurement accuracy was:

- $\Delta x = 0.1$ mm for RGA translations, and
- $\Delta \alpha = 3.6$ arcseconds for RGA rotations.

This fundamental instrumental uncertainty propagated to uncertainty in the positions of optical hardware. As an example, the results of three different measurements of the same position (point F) were performed using three different detectors. The results of this measurement were:

Detector	x	y	z
Jet/X	-6350.4	-0.10	-0.10
PSPC	-6351.7	-0.91	-0.60
RFC	-6350.6	-0.73	+0.73

Table 6: Three measurement results of the same point using different instruments

An ideal set of measuring equipment would yield identical numbers in each column. These measurements yield a set of the fundamental minimum uncertainty better than which hardware positions at Panter cannot be determined:

- $\Delta x = 0.2$ mm
- $\Delta z_F \simeq \Delta y_F \simeq 1$ mm.

3.3.2 Apparatus positioning reproducibility

It was found that when an optical apparatus was moved out of a known position and then back into it, there would be a spread in the final measured position. Moreover, any time one piece of apparatus on the optical bench (either the mirror module or the RGA) was moved, the other piece would show some motion. The following list summarizes the results of a set of dedicated measurements to measure these effects.

- Mirror Module
 - $\Delta z_{MM} \lesssim 2$ mm
 - $\Delta y_{MM} \lesssim 1$ mm
- RGA
 - $\Delta z_{RGA} \lesssim 1$ mm
 - $\Delta y_{RGA} \lesssim 0.3$ mm
 - $\Delta el_{RGA} \lesssim 25$ arcseconds,

where el_{RGA} is the elevation angle of the RGA.

The numbers above are the worst-case possibilities which are obtained when the piece of equipment itself is moved. That is, when the mirror module is moved, the expected uncertainties in the mirror module's position are the number quoted above, Δz_{MM} and Δy_{MM} . The RGA will likely have suffered some movement, but of smaller amounts than the RGA values listed.

Another set of dedicated measurements compared the positions of the RGA before the entire April 1998 campaign with the positions after the entire April 1998 campaign. The observed movement was very slight, all within the above quoted measurement uncertainties. This result implies that the apparatus positioning reproducibility uncertainties were not "random walking" away from the expected positions. The values obtained from this set of measurements are:

- $\Delta \alpha_z = 0.72$ arcseconds
- $\Delta el = 1.0$ arcseconds
- $\Delta x_{G'} = 1.0$ mm
- $\Delta y_{G'} = 0.01$ mm
- $\Delta z_{G'} = 0.07$ mm

3.3.3 Spot position predictability

After positioning all the hardware for a given measurement, there nearly always remained a difference between the measured and predicted spot positions. The source of this difference could only be assigned to the integrated uncertainty due to all mispositionings. For any single measurement, there was no way to discern the source of a small observed discrepancy in measured versus predicted spot position.

Since some mispositionings would show predictable trends from order to order, software was developed to detect such mispositionings, subject to overall measurement uncertainty. "Tamsop" is a program that takes encoder values and alignment information of a given measurement to determine the spot location in theodolite coordinates. Known mispositionings can be taken into account, and some unknown mispositionings were found when their effects had well pronounced trends. Small residual uncertainties between predicted and measured spot positions remained. [6]

Columbia Astrophysics Laboratory	XMM-RGS	Doc.: RGS-COL-CAL-98027 Page: 18 Auth.: Joshua Spodek Date: December 21, 1998
---	----------------	--

The following numbers represent the maximum uncertainties in the determinations of the RGA and the RFC positions, when reduced by Tamsop:

- December 1997 campaign:
 - $\Delta z_{\text{spotpos}} \approx 0.3$ mm
 - $\Delta R_{y_{RGA}} \approx 6.6$ arcseconds
 - $\Delta z_{RGA} \approx 0.25$ mm
- April 1998 campaign:
 - $\Delta z_{\text{spotpos}} \approx 0.5$ mm
 - $\Delta R_{y_{RGA}} \approx 7.2$ arcseconds
 - $\Delta z_{RGA} \approx 0.23$ mm

Note that Tamsop is not sensitive to Δx_{RFC} .

3.4 Mechanical Tolerancing on Grating Positions

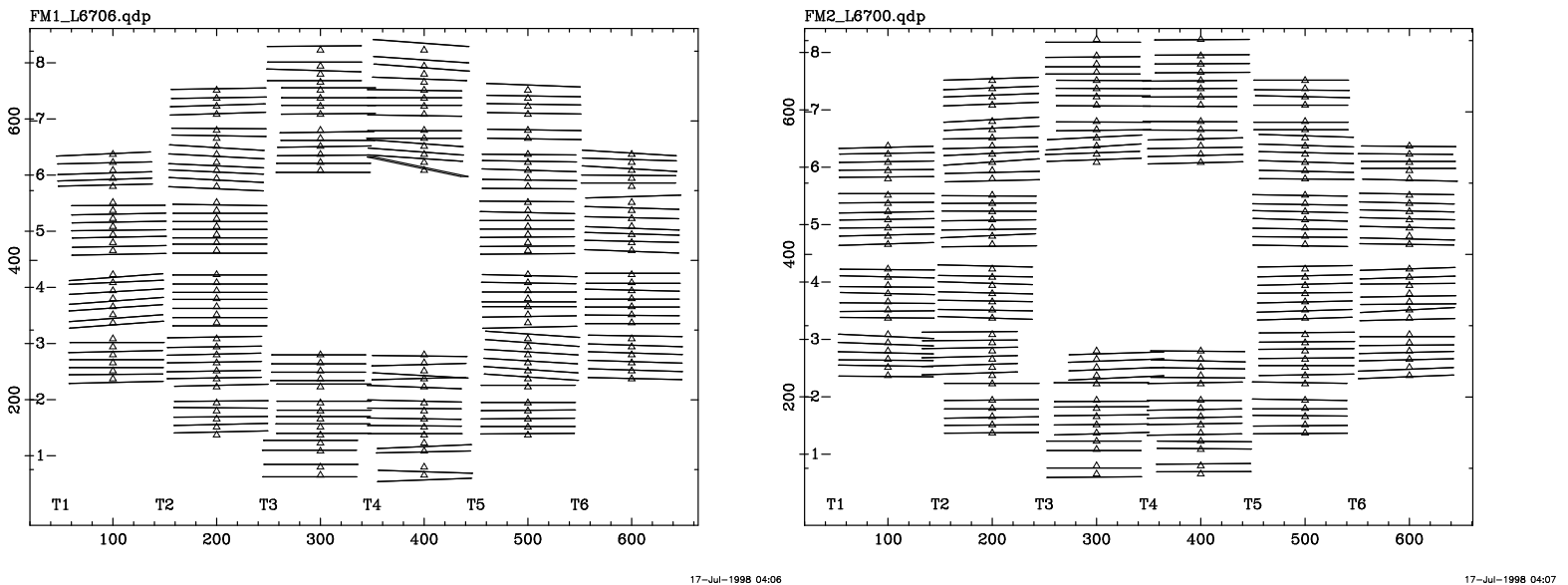
3.4.1 Assembly room data: individual grating misalignments and bow

Detailed individual grating flatness information was taken interferometrically prior to assembly with the integrating structure. Detailed individual grating position information was taken during RGA assembly. The data was taken as twists of each side of each grating plus the measured grating bow—that is, five numbers per grating. The data was saved in the form of 4 grating corner perturbations plus the grating bow. These numbers are incorporated internally in the physical model as R_y , R_x , T_z , grating twist, and grating bow.

The detailed information of grating corner perturbations ($(181 + 182) \times 4$ numbers) for each RGA is presented in figure 6, in a rather dense format. Figure 7 shows histograms of the misalignments in the dispersion direction, which affects the PSF most directly. Figure 7 is significantly easier to read, although it contains less information than figure 6.

Figure 8 shows histograms of the grating bows as measured during the assembly process. Only the bow in the dispersion direction, which is the direction of the bow in the plots, is used on a per-grating basis in the physical model. The cross-dispersion bow is implemented as an average of the measured bows.

As the physical model is actually implemented, all the available information on grating misalignments and bow is used on a per-grating basis. That is, each grating in the model of each RGA is misaligned and endowed with a bow by the amounts measured during the assembly process. The histograms in figures 7 and 8 are histogrammed for heuristic purposes and do not contain as much information as the physical model.



17-Jul-1998 04:06

17-Jul-1998 04:07

Figure 6: A pair of plots, each of which displays all the measured misalignment values for each RGA box, RGS2/RGA1 on the left, RGS1/RGA2 on the right. The triangles show the ideal grating position, and a set of horizontal lines centered on the triangles would represent an ideal RGA. Each line can be displaced in three ways, two translations and one rotation, which represent three types of misalignments. A vertical shift represents a misalignment in $\Delta\alpha$ —that is, the dispersion direction—which has the greatest effect on the PSF. A horizontal shift represents a misalignment in the cross-dispersion direction. A rotation of the line represents a grating twist.

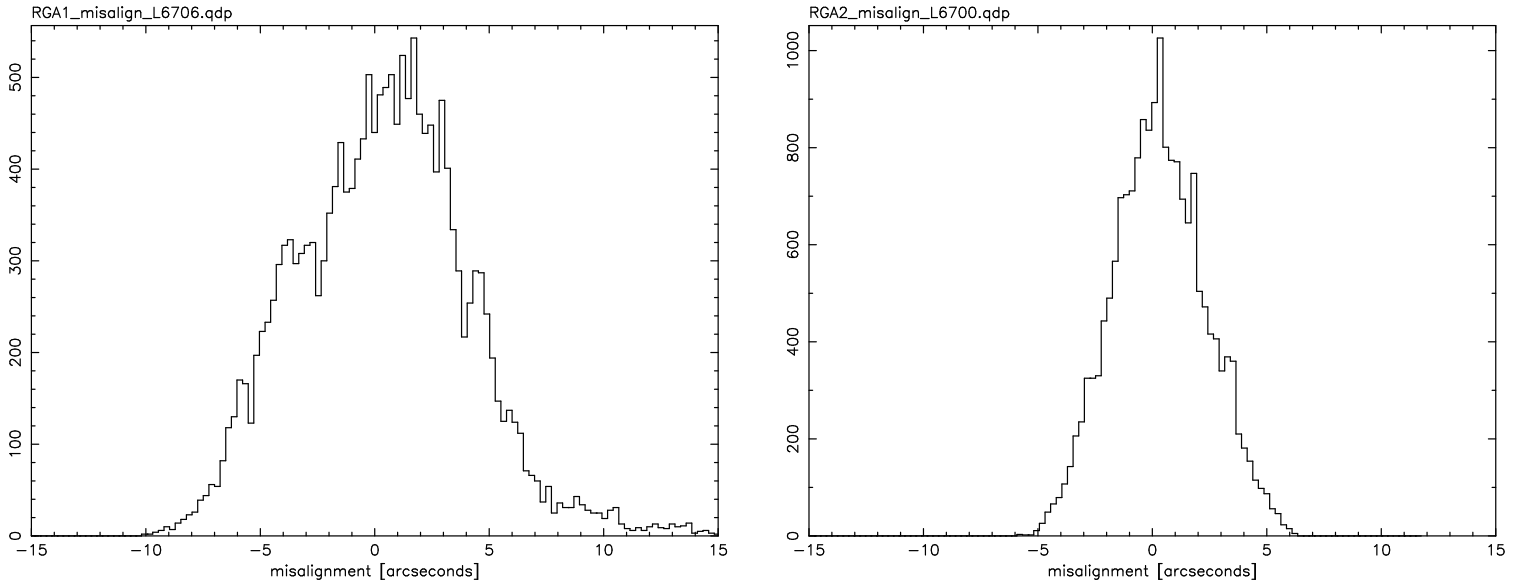


Figure 7: A pair of histograms of grating misalignments of rotations in the dispersion direction, the perturbation that affects the PSF most directly. In the previous figure (6) this misalignment is represented by a vertical shift. Again, RGS2/RGA1 is on the left and RGS1/RGA2 is on the right.

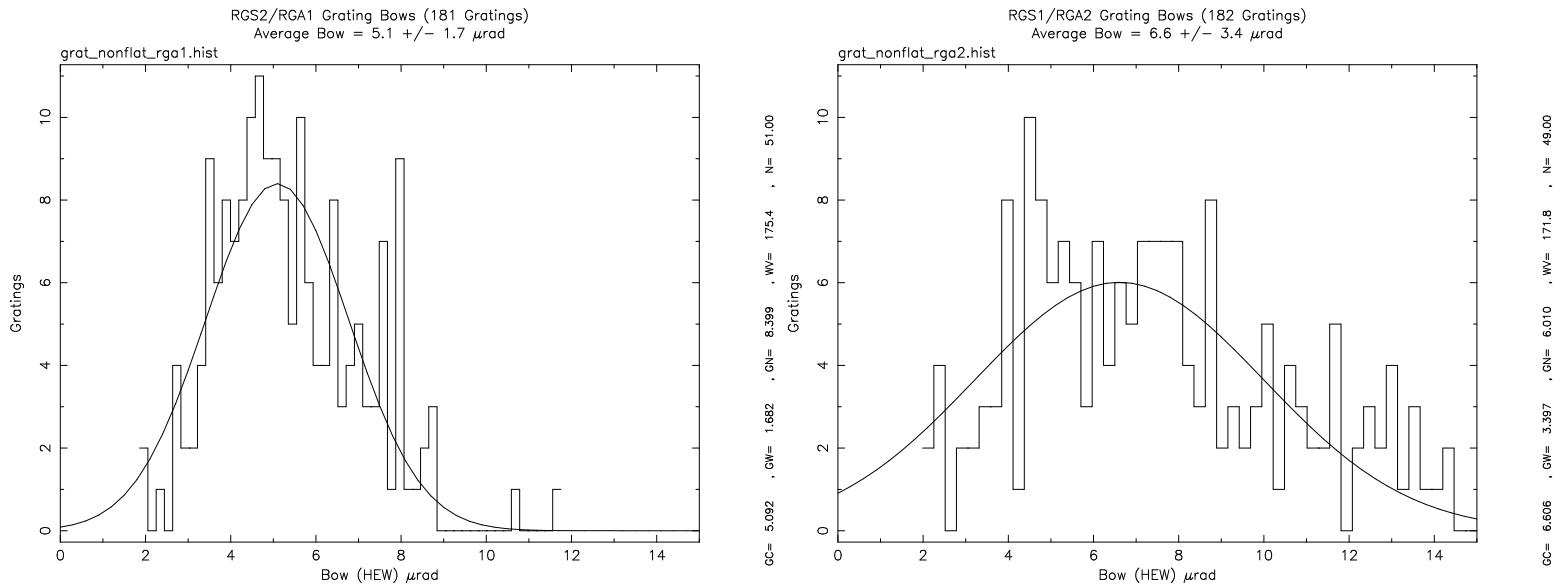


Figure 8: A pair of histograms of grating bow in the dispersion direction, the direction that directly affects the PSF. Again, RGS2/RGA1 is on the left and RGS1/RGA2 is on the right.

Columbia Astrophysics Laboratory	XMM-RGS	Doc.: RGS-COL-CAL-98027 Page: 21 Auth.: Joshua Spodek Date: December 21, 1998
---	----------------	--

Unmeasured during the assembly process are the physical parameters listed below, whose effect on the PSF is virtually negligible. The width of the distributions used to describe these parameters is given, although the exact numbers are educated guesses based in order of magnitude on the experience of the assembly room workers. For these parameters to cause observable effects in the PSF would require multiple orders of magnitude increases, into the range of visually observable misalignments, which were not observed.

- $\Delta y_{\text{grat}} = \pm 1\text{mm}$
- $\Delta x_{\text{grat}} = \pm 0.3\text{mm}$
- $R_z = 1$ arcmin (Rotation about dispersion axis)

RGS2/RGA1 was assembled with systematic interferometer error, which was later understood and modeled (see [10]). That model depended on the unknown parameter θ_0 , determined after the fact at Panter. Its derivation will be discussed in section 4.1.

3.4.2 Machining Specifications

Table 7 lists the precision that was specified to the manufacturers of the components of the RGA along with the verification performed to validate the precision.

item	tolerance	verification
Top rails	Aligned to $\pm 0.15\mu\text{m}$ (flat distribution)	Sandia coordinate measuring machine
Bottom rails	Aligned to ± 1 arcsec with respect to the corresponding top rail (flat distribution; this is where the interaction with the grating flatness term in the budget would come in)	Nevis Zygo interferometer
Bosses	Machined to $\pm 1.2\mu\text{m}$ (flat distribution)	Moore Tool coordinate measuring machine
Absolute embedment	Flat distribution between 0.5 and 2.5 μm (does not affect assembly angular alignment budget, only the absolute locations of the gratings on the Rowland circle)	Model verified by controlled experiment at LLNL
Differential embedment	Half occurs during assembly and is therefore already accounted for in the 1 arcsecond tolerance of the rail alignment. The other half develops over timescales of years and should therefore be kept as a random term when studying the performance of the RGS on the spacecraft	Verified by analysis
Line spacing	Specification to Perkin-Elmer of 3 Å	Interferometrically controlled ruling engine

Table 7: Machining specifications for subcontracted parts.

<p>Columbia Astrophysics Laboratory</p>	<p>XMM-RGS</p>	<p>Doc.: RGS-COL-CAL-98027 Page: 22 Auth.: Joshua Spodek Date: December 21, 1998</p>
--	-----------------------	--

3.5 Scattering Model

The derivation and validation of the model to describe scattering from a single grating due to surface microroughness is described in [7]. Only small angle scatter is considered here, as it relates to the PSF, although the theory also predicts wide angle scatter. On the angular scale of a single line, the wide angle scatter observed on the XMM gratings appears simply as lost light, with no effect on the single line's core profile. Wide angle scatter is therefore not considered here. Small angle scatter as observed on the XMM gratings gives the profile extended wings that broaden the core and alter its shape.

The scattering theory predicts both the shape of the scattering wings and the fraction of the core that is scattered into the wings. This prediction is based on two free parameters which depend on the average properties of a single grating: the root mean square height of the grating's microroughness, σ , and the correlation length of that roughness, l . The angular distribution of the scattered light, $\frac{1}{\eta_m} \frac{d\eta}{d\beta}$, and fraction of scattered light, TIS , are predicted by

$$\frac{1}{\eta_m} \frac{d\eta}{d\beta} = \frac{(\sin \alpha + \sin \beta)^4}{(\sin \alpha + \sin \beta_m)^2} \sin \beta_m k^3 W(p, \sigma, l) \quad (2)$$

$$TIS = 1 - \frac{2}{e^{2k^2 \sigma_{eff}^2 (\sin \alpha + \sin \beta)^2} + 1}, \quad (3)$$

where

- m = order into which the light is scattered,
- α = angle of incidence of light,
- β = exit angle of light,
- k = wavenumber,
- $p = k(\cos \alpha - \cos \beta)$,
- W = "power spectral density function," contains the distribution of microroughness of the grating,

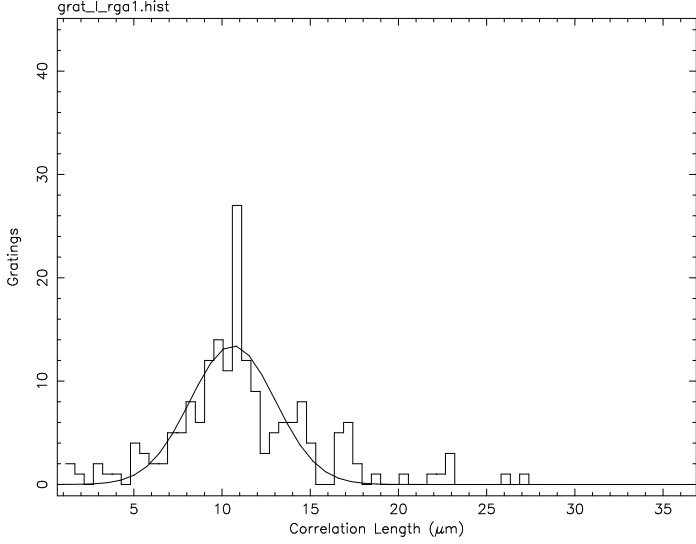
and β_m satisfies the grating equation,

$$\frac{m\lambda}{d} = \cos \alpha - \cos \beta \quad (4)$$

for a given α , $k(= \lambda/2\pi)$, and m . W has been found to be well-described by analytical distributions. The XMM gratings have, in practice, been characterized by W proportional to a Gaussian distribution.

The single grating testing campaign at Columbia's Nevis Labs has determined the scattering parameters, σ and l , for 90 percent of the gratings used in the two RGAs. Figures 9–10 show the distributions of each scattering parameter for each RGA.

RGS2/RGA1 Grating Correlation Length (181 Gratings)
 $l_{ave} = 10.6 \pm 2.4 \mu\text{m}$



RGS1/RGA2 Grating Correlation Length (182 Gratings)
 $l_{ave} = 11.1 \pm 1.6 \mu\text{m}$

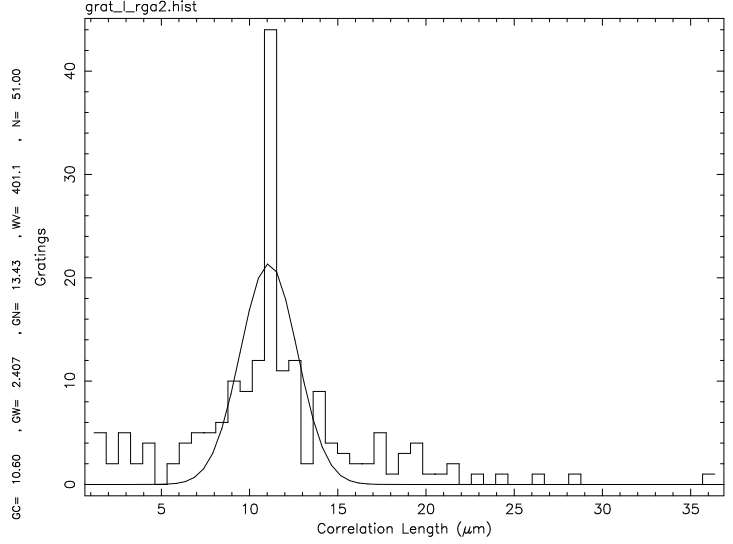
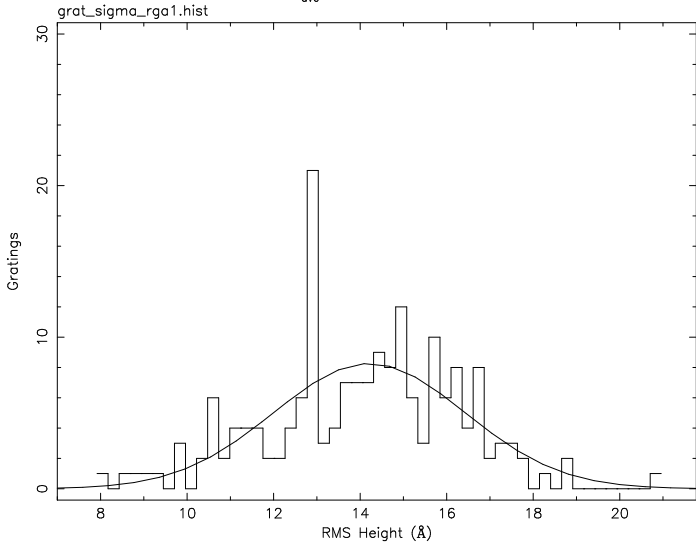


Figure 9: Histograms of grating microroughness correlation lengths for each RGA. RGS2/RGA1 is on the left, RGS1/RGA2 is on the right. See text about the spikes at $10.9 \mu\text{m}$

RGS2/RGA1 Grating RMS Height (181 Gratings)
 $\sigma_{ave} = 14.2 \pm 2.2 \text{ \AA}$



RGS1/RGA2 Grating RMS Height (182 Gratings)
 $\sigma_{ave} = 14.2 \pm 2.5 \text{ \AA}$

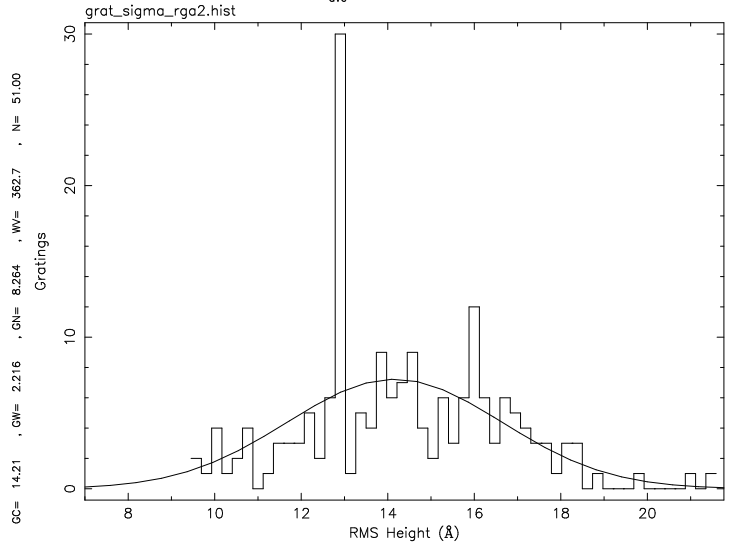


Figure 10: Histograms of grating microroughness root mean square height for each RGA. RGS2/RGA1 is on the left, RGS1/RGA2 is on the right. See text about the spikes at 12.8 \AA .

Data for the remaining 10 percent of the gratings has suffered corruption (although the gratings themselves suffered no corruption). The scattering parameters for those gratings have been set to average values. The average for σ included information from the RGA Engineering Qualification Model (EQM). As noted in [7], EQM testing at Panter measured grating scatter in ranges of parameter space unattainable with the Nevis equipment and beyond the applicable range of the new theory.

The reason for including the EQM information is as follows. As expected for an array of gratings, the scattering behavior for the EQM was slightly different than expected for a single grating in the new parameter space. The exhibited scattering behavior was easily incorporated empirically into the theory, but yielded a slightly different σ than that measured at Nevis. Since both sets of measurements—Nevis and EQM—were equally valid, the EQM information was averaged with the Nevis information for the gratings whose data was corrupted.

Explained fully in [7], figure 11 displays the data used to determine σ for the array EQM array. Points to the right, at high k and β , require brighter sources and higher integration times than were attainable or feasible in the Nevis campaign.

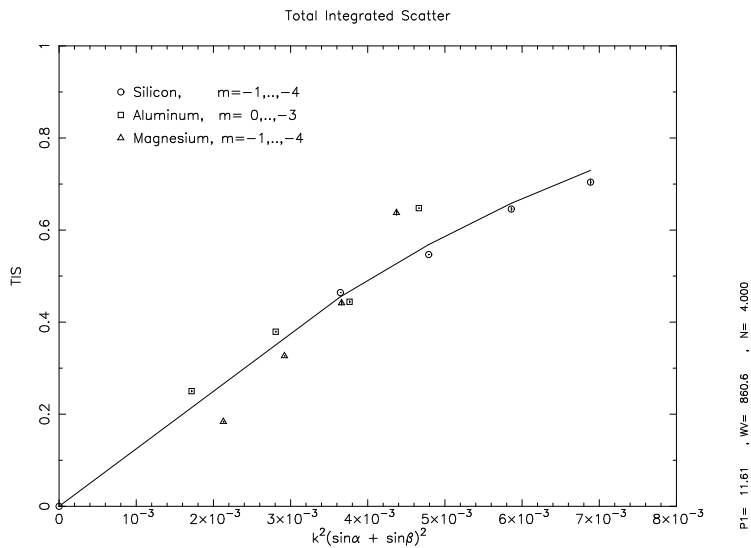


Figure 11: EQM data used to evaluate the scattering theory at extreme ranges of parameter space. The points to the right are unattainable with Nevis equipment, but are useful to constrain and extend the scattering theory.

The gratings with the averaged values give the spikes in figures 9 and 10. The spikes are off-center in figure 10 due to the EQM averaging.

As the physical model is actually implemented, all the available information on scattering parameters is used on a per-grating basis, as with the misalignment and bow information. That is, each grating in the physical model of each RGA has associated with it the proper scattering parameters as measured at Nevis.

As a check for correlation between the scattering parameters, figure 12 displays a scatter plot of σ versus l for each grating. Little correlation is evident between the two parameters. On the other hand, slight correlations did exist between the small angle scattering parameters and the large angle scattering parameters. Since large angle scattering parameters were used to discriminate and reject poor gratings—those with low l and high σ —abrupt cutoffs are evident in this plot at low l and high σ .

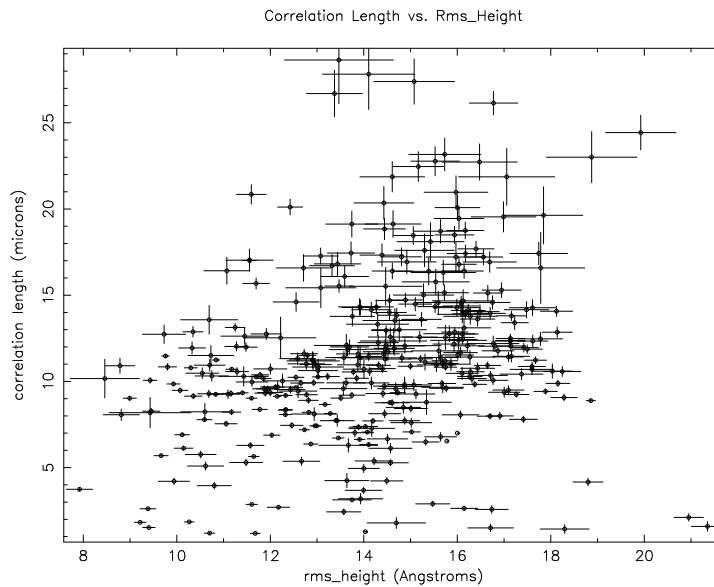


Figure 12: Scatter plot of the small angle scattering parameters measured at Nevis.

Columbia Astrophysics Laboratory	XMM-RGS	Doc.: RGS-COL-CAL-98027 Page: 26 Auth.: Joshua Spodek Date: December 21, 1998
---	----------------	--

4 Review of measurement results

This section presents the results of the Panter measurements. Presented first is the RGS2/RGA1 data, taken in August and December 1997, followed by the RGS1/RGA2 data, taken in April 1998. The data is presented in both subsections in the order

1. Focus Searches
2. Gluecksrad Results
3. The Problem with RGA1 (RGS2/RGA1 only)
4. Gluecksrad Composites
5. Full Box Results

Item 3 is required for the first-built RGA only. That RGA was built with a malfunctioning interferometer, which resulted in misalignment errors for each grating. These misalignments were found, corrected, and tested with gluecksrad measurements, as described in that section.

4.1 RGS2/RGA1

4.1.1 Focal searches

Figure 13 displays an example of a focus search result from the RGS2/RGA1 test (full results are in [8]). Both plots show the spot size as a function of detector position relative to the nominal Rowland circle position. The top plot shows simulated data based on the physical model. The bottom plot shows Panter data. Both plots show a broad minimum nearly a centimeter wide in the dispersion direction.

The fitted model is

$$HEW(x) = \sqrt{HEW^2(x_o) + F^2(x - x_o)^2}, \quad (5)$$

where HEW is the half energy width, x is the direction toward or away from the RGA, F is the focal length of the RGA, and x_o is the position of best focus. This model contains an estimated 1–2 mm systematic uncertainty in its determination of best focus.

Useful comparisons may be made both between dispersion and cross dispersion minimum in the Panter data and in the same direction between simulated and real data.

The averages over all focal searches are as follows (excluding monochromator data):

- $\overline{x_o}(\text{data}) = 1.56 \text{ mm}$
- $\overline{x_o}(\text{model}) = 1.00 \text{ mm}$
- $\Delta\overline{x_o}(\text{data-model;cross-dispersion}) = -0.97 \text{ mm}$,

Columbia Astrophysics Laboratory	XMM-RGS	Doc.: RGS-COL-CAL-98027 Page: 27 Auth.: Joshua Spodek Date: December 21, 1998
---	----------------	--

where the average positions for both data and model should have been 1.00 mm due to known misalignments.

The conclusion in [8]: “The averages are all well within the depth of focus range, indicating that all the profile data were taken essentially in focus.”

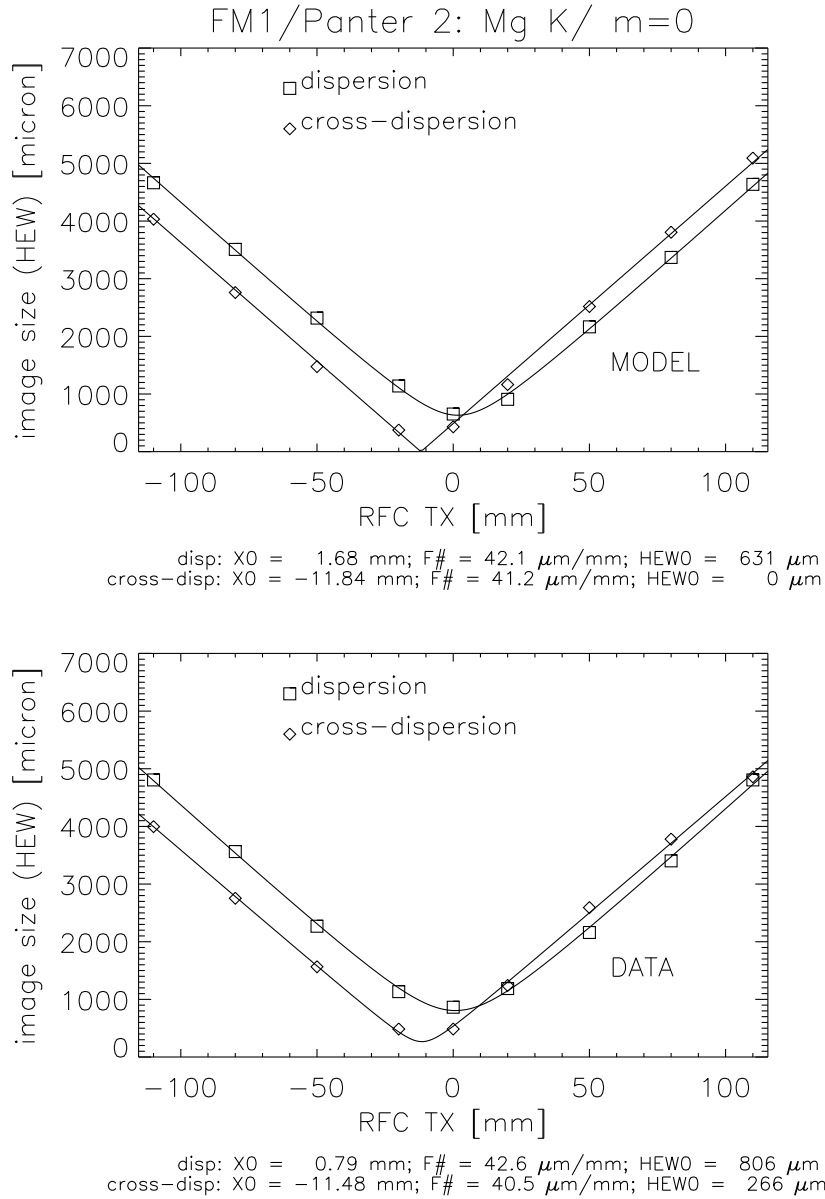


Figure 13: A sample focus search from RGS2/RGA1. Top: Simulated data based on the physical model, dispersion and cross dispersion. Bottom: Panter data, dispersion and cross dispersion. Comparison may be made between simulated versus actual data in each direction, as well as between directions.

4.1.2 Gluecksrad results

The reader is referred to section 2.2 for sample plots of gluecksrad profile comparisons as well as the map of gluecksrad aperture positions. In the interest of brevity, those are the only such plots included (of the 60+ such plots available) in this document. A full sample of such plots from RGS2/RGA1 are available in [9].

Figure 14 shows a plot of spot centers for the full set of RGS2/RGA1 gluecksrad measurements from the August 1997 Panter run. Figure 15 displays the same data in four separate plots, separated by gluecksrad radial sector. In these plots the horizontal axes represent the angular position of the gluecksrad aperture illuminating the CCD. The vertical axes represent the linear offset on the CCD of the spot center.

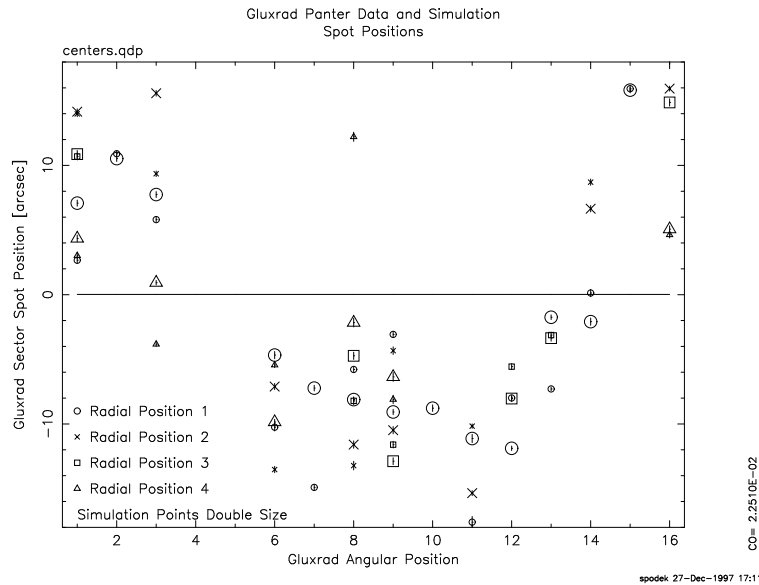


Figure 14: Plot of all gluecksrad spot centers. The horizontal axis shows the sector number, which is proportional to ϕ_{RGA} , the polar angle around the RGA. The vertical axis shows the linear offset of the spot center with respect to the overall average. The sinusoidal trend in ϕ_{RGA} is equivalent to a linear trend in z_{RGA} . Large markers represent centers of simulated data, small markers represent centers of real data.

The obvious sinusoidal trend of the spot centers in angular position of gluecksrad aperture is equivalent to a linear trend in the z position of the gluecksrad aperture position. The same plot of an ideal RGA would show all centers randomly distributed about the horizontal line at 0.

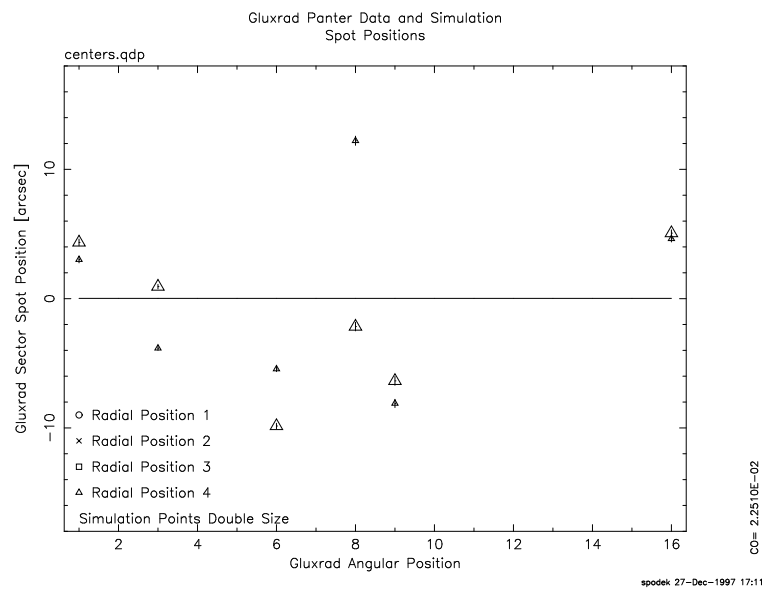
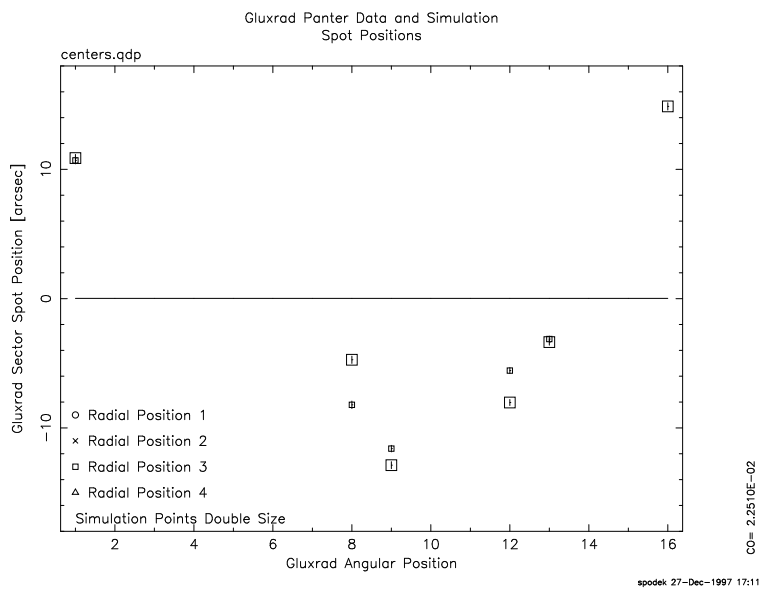
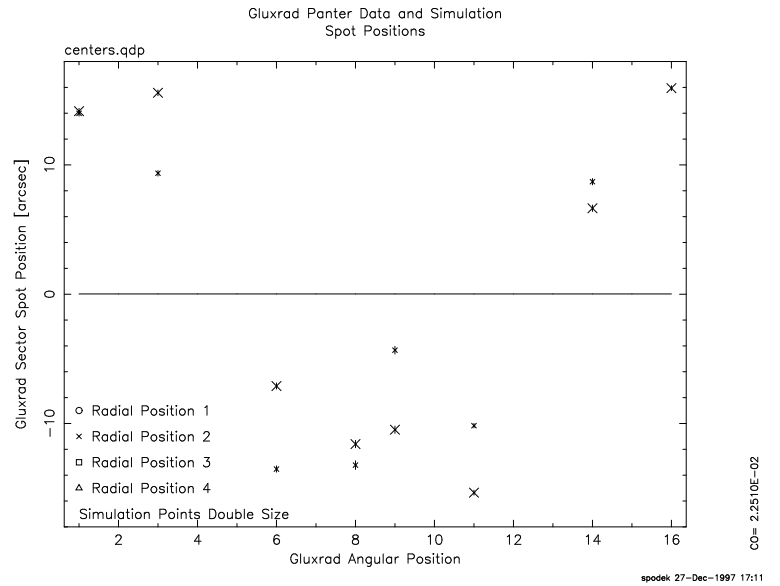
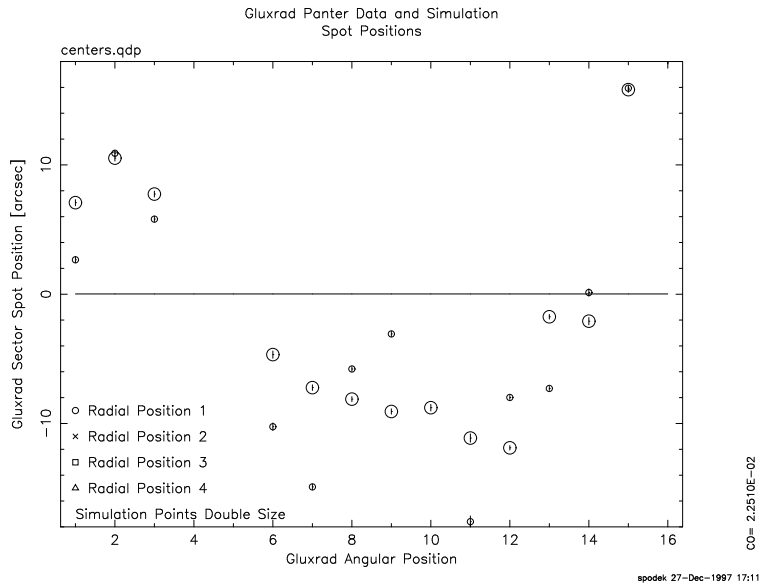


Figure 15: Same as previous figure, but separated by the four gluecksrad angular sectors.

4.1.3 The problem with RGA1

The problem with RGA1, which was diagnosed only after the final and irrevocable assembly, was that it was assembled with a malfunctioning alignment interferometer. This diagnosis, and the modeling of the resulting misalignment, are detailed in [10] and [14]. The result of the misalignment is a too slight change in fan angle from grating to grating in the RGA. In other words, the gratings are too parallel, which is consistent with the linear trend in z along the RGA.

The incorporation of the model of this misalignment into the overall physical model successfully approximates the observed behavior of RGS2/RGA1. This behavior is evidenced in the cosinusoidal trends in figures 14–15, as well as the lack of any such trend in the residuals, shown in figures 16–17. These plots are similar to figures 14–15, but plot the differences between simulated and real data spot centers.

As expected of a correct diagnosis, the dispersion of the residuals is smaller than the dispersion of the actual spot centers. The nature of the outlier at sector 8,4 that is poorly described by the model remains poorly understood. Unlike the outlier in sector 10,1 (which was displayed in section 2.2), whose misalignment was visible to the naked eye and modeled, the gratings in this sector are not visibly misaligned. Since the spot in the Panter data shows no increased dispersion, the gratings within that sector appear to be coherently misaligned—that is, not shaken out of place, but somehow incorrectly assembled. But no existing measurement has resolved the nature of the misalignment. Barring future testing, which is unlikely, the few percent of the X-rays incident on these gratings will remain modeled as shown here.

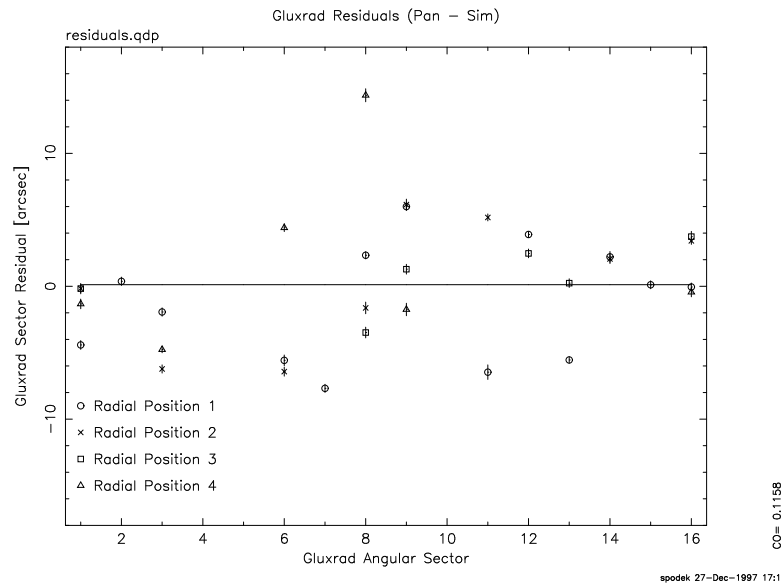


Figure 16: Plot of all gluecksrad spot center residuals. The axes are the same as the previous plots.

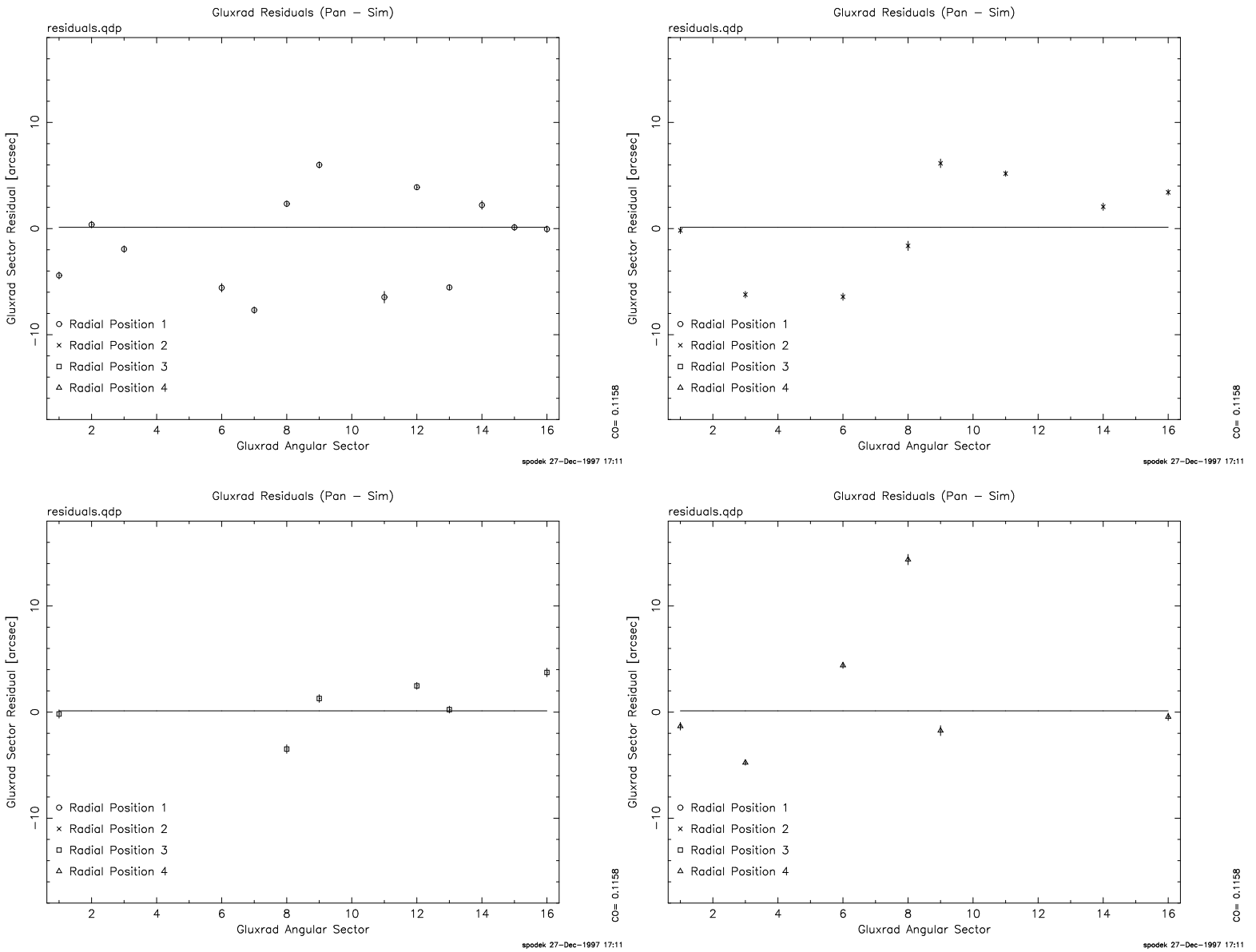


Figure 17: Same as previous figure, but separated by the four gluecksrad angular sectors.

4.1.4 Gluecksrad composites

The modeling of the interferometer misalignment involved one unmeasurable parameter. As explained in [10], this parameter is the original angle, θ_o , at which the RGA was held during the grating insertion process. Rotating the RGA from this angle to the next for the insertion of later gratings at each's appropriate angle, and thereafter to all future angles, propagated a small misalignment. The later misalignments were calculable, but all depended on the original angle, which was not recorded. Assembly room workers recalled the angle to be approximately 2.3° , or γ_{design} , the nominal graze angle for the grating at blaze.

With no physical measurement to determine θ_o , the only choice was to fit it with the Panter data, despite such fitting not being the original purpose of the Panter tests. Since different choices in θ_o yielded different distributions in the large markers in figures 14–15, different θ_o 's would also yield different distributions in the residuals in figures 16–17.

Figure 18 shows a histogram of the residuals in figures 16–17 for $\theta_o = 2.35^\circ$, with a Gaussian overlaid. The hypothesis was made that the θ_o that resulted in the smallest dispersion of residuals was most likely the θ_o actually used during assembly.

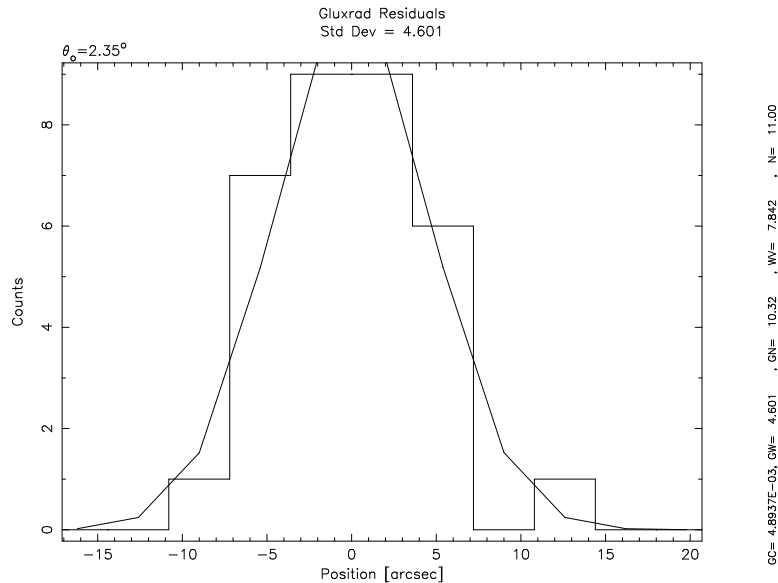


Figure 18: Histogram of the residuals in the previous figures with a Gaussian overlaid.

Sample simulations were (laboriously) performed over a range of θ_o about the value recalled by the assembly room workers. For each simulation a set of gluecksrad residuals and its dispersion was (laboriously) calculated. Figure 19 shows the dispersions as a function of θ_o , showing a broad flat minimum in the expected range. The value of 2.35° was chosen for the two-fold reason that it was the global minimum, though just barely, and that it was the closest to γ_{design} .

The simulation results plotted in this section and the preceding section were only those resulting from a

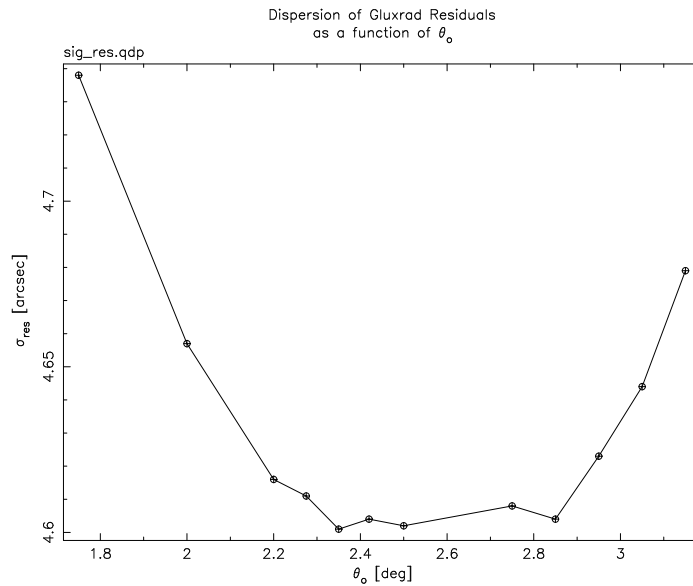


Figure 19: Plot of the value of the dispersion of the gluecksrad residuals as a function of θ_o about the range recalled by the assembly room workers.

choice of $\theta_o = 2.35^\circ$. The decision to exclude the other results was in the interest of brevity, with the understanding that figure 19 contained the most important information of the other results.

Columbia Astrophysics Laboratory	XMM-RGS	Doc.: RGS-COL-CAL-98027 Page: 35 Auth.: Joshua Spodek Date: December 21, 1998
---	----------------	--

4.1.5 Full box results

As noted in section 2.3, the full box profiles were chosen for having the following properties, which lend them high diagnostic power:

- High energy lines,
- Narrow lines,
- High order,
- High scatter,

and are plotted with logarithmic scaling on vertical axis. All of these properties and the scaling conspire to make the profiles *look* worse on the page. The reader is therefore reminded when looking at *apparently* broad lines that this appearance is either superficial or a sign of just how great the diagnostic power of a given plot is.

Lines of high $|m\lambda|$, which were used to obtain PSF data at higher β , are generally not of astronomical interest. The high scatter seen here is not completely representative of what would be seen with longer wavelength, lower order illumination which would be diffracted to the same β and would be of more interest in actual XMM observations.

Also as noted in section 2.3, the χ^2 values quoted with each plot do not refer to a fitting that allowed a change in profile shape. The χ^2 minimization only varied recentering and renormalization of the simulated profile relative to the profile resulting from real Panter data. These parameters do not affect the shape of the profile.

All plots are shown $-4 < \Delta z < +4$, which was the region over which fitting was performed. The scale in y is constant for each profile of a given source, but varies from source to source. Binning is performed to a minimum of ten counts per bin for proper χ^2 statistics. All simulation hardware positions are according to encoder values from Panter measurements, sometimes given greater accuracy if possible through Tamsop.

The following full box results are presented for RGS2/RGA1:

1. Al, "A" configuration, $m=0,-1,-2$
2. Mg, "A" configuration, $m=0,..,-4$
3. Al, "B" configuration, $m=0,..,-3,-4$
4. Mg, "B" configuration, $m=0,..,-3$

The "A" configuration is the nominal Panter configuration. The "B" configuration has RGA moved back 6.0 mm from the nominal configuration with no rotation to approximate the true flight configuration for this grating array. This configuration partially corrects the interferometer-caused error discussed above, and in more detail in [11]

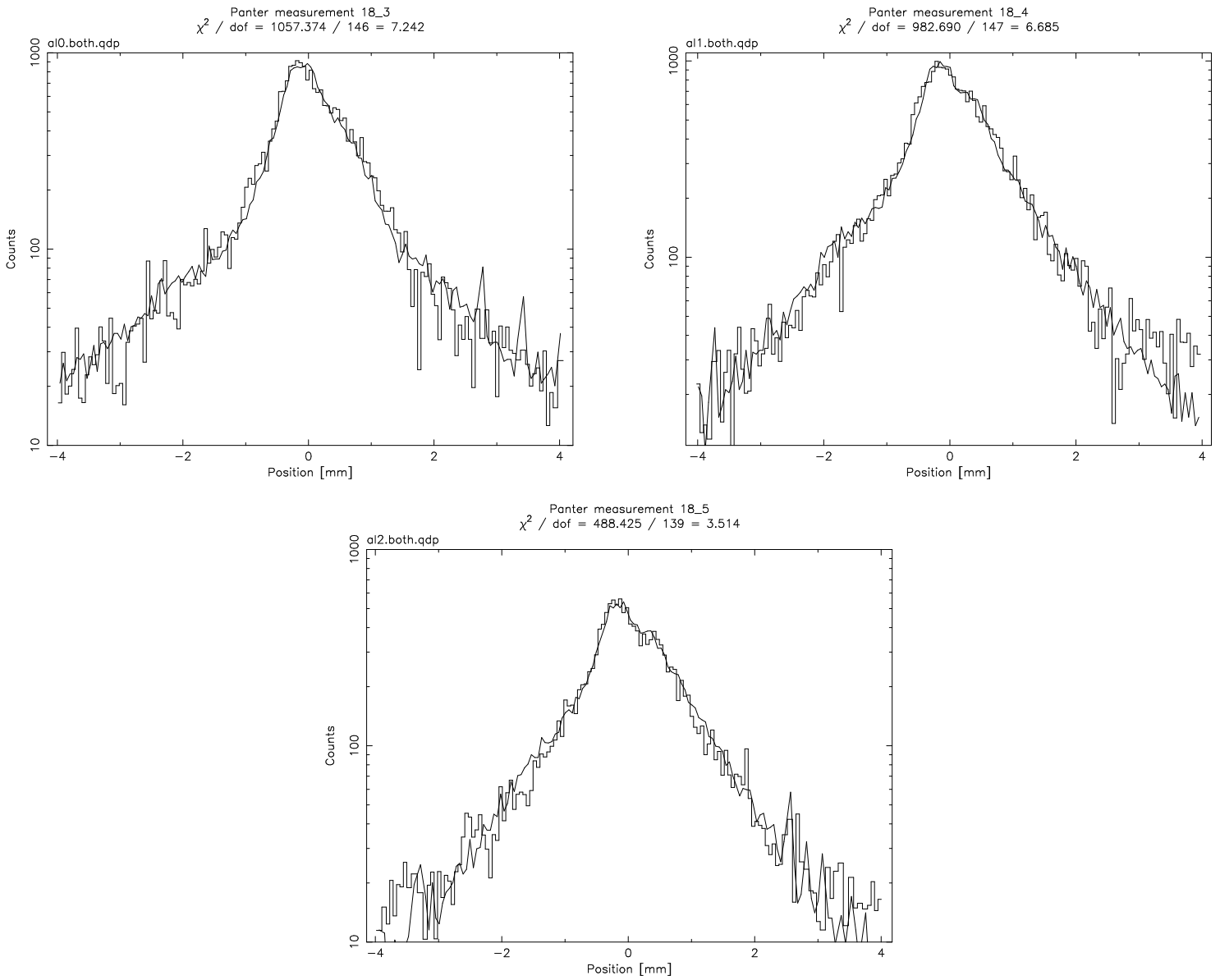


Figure 20: Plots of the full box Al K data from RGS2/RGA1, configuration A.

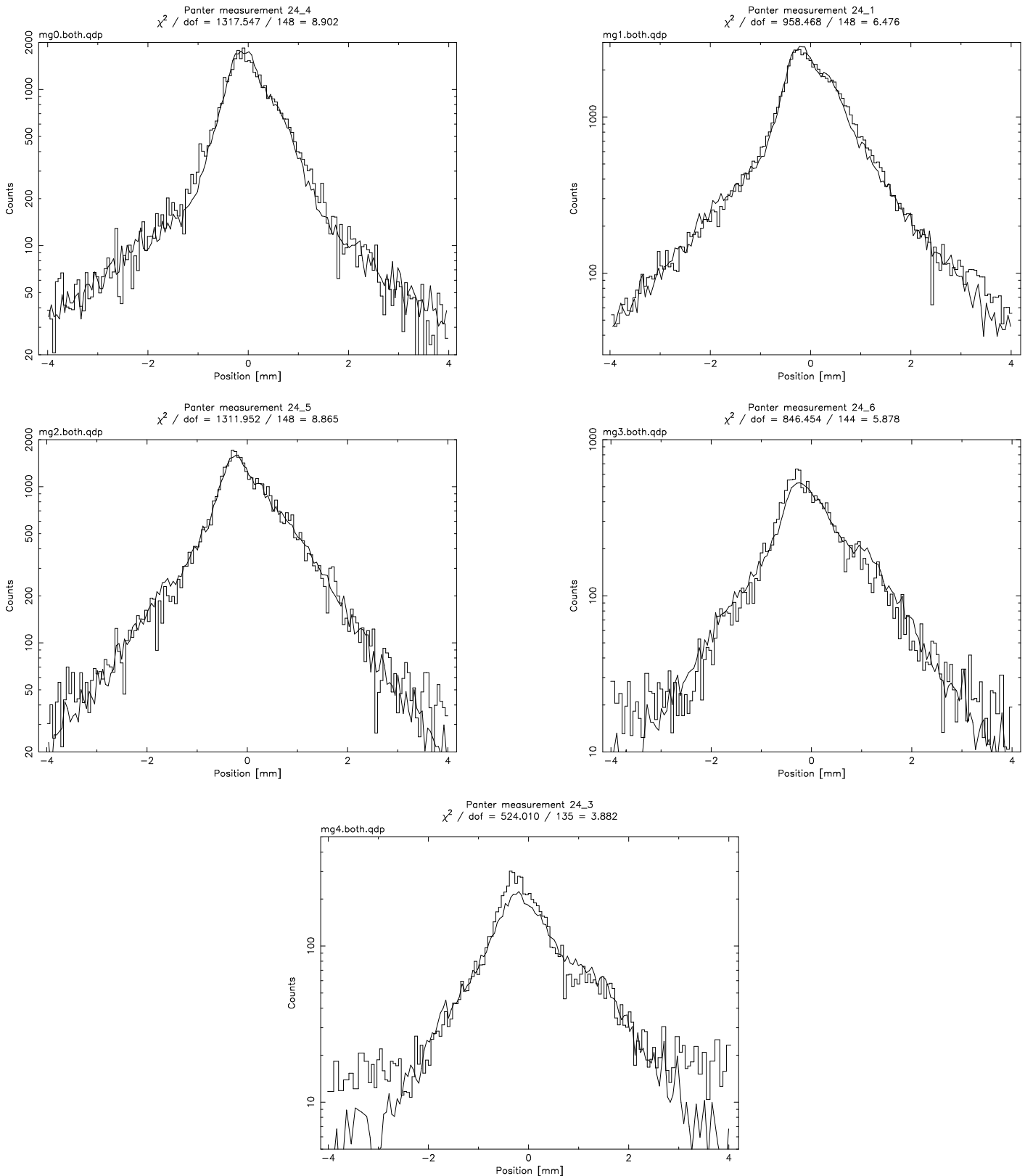


Figure 21: Plots of the full box Mg K data from RGS2/RGA1, configuration A. In the highest order profiles, where the fraction of scattered light is large (>50%), first order scattering theory breaks down in predictions of both scattering fraction and profile shape. The consistency between data and model is about as good as can be expected.

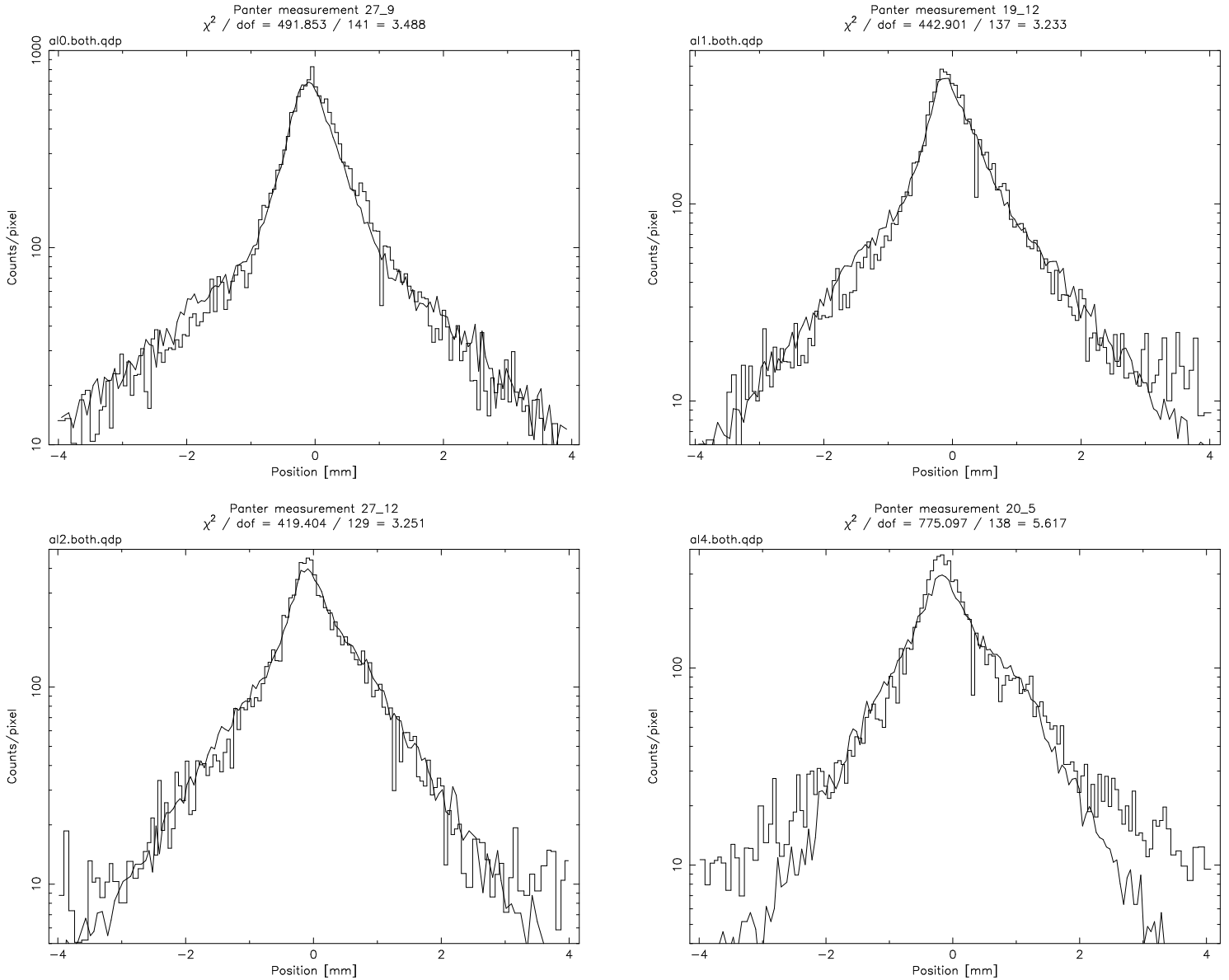


Figure 22: Plots of the full box Al K data from RGS2/RGA1, configuration B. In the highest order profiles, where the fraction of scattered light is large (>50%), first order scattering theory breaks down in predictions of both scattering fraction and profile shape. The consistency between data and model is about as good as can be expected.

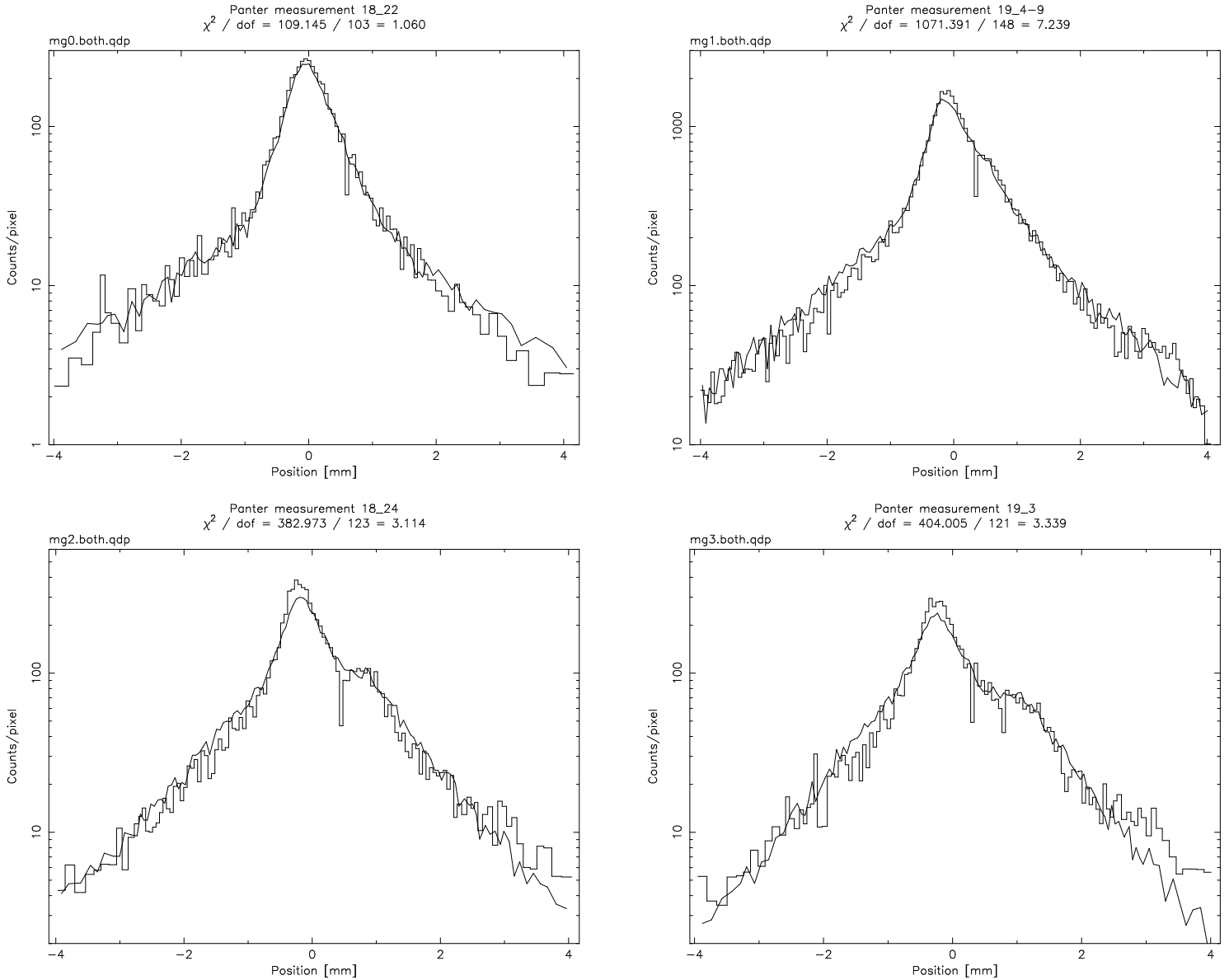


Figure 23: Plots of the full box Mg K data from RGS2/RGA1, configuration B. In the highest order profiles, where the fraction of scattered light is large (>50%), first order scattering theory breaks down in predictions of both scattering fraction and profile shape. The consistency between data and model is about as good as can be expected.

4.2 RGS1/RGA2

4.2.1 Focal searches

Figure 24 displays two examples of focus searches from the RGS1/RGA2 test. Both plots show the spot width as a function of detector position relative to the nominal Rowland circle position. Panter data and simulated data are overlaid. Both are fitted with the same model as in the RGS2/RGA1 test, equation 5. The same 1–2 mm systematic uncertainty is introduced by this model. No cross dispersion comparisons were made. The averages over all focal searches are as follows:

- Mg average positions (should be -0.75 mm due to known hardware misalignments):
 - $\overline{x}_o(\text{data}) = 0.68$ mm
 - $\overline{x}_o(\text{model}) = -0.89$ mm
- O average positions (should be 0.0 mm):
 - $\overline{x}_o(\text{data}) = -0.47$ mm
 - $\overline{x}_o(\text{model}) = -0.47$ mm

The hardware misalignments for the Mg focal searches are discussed, with slight disagreement, in [12], [13], and [5]. For the purposes of the PSF measurements, the focal searches showed that the averages were within the depth of focus range, indicating that all the profile data were taken essentially in focus.

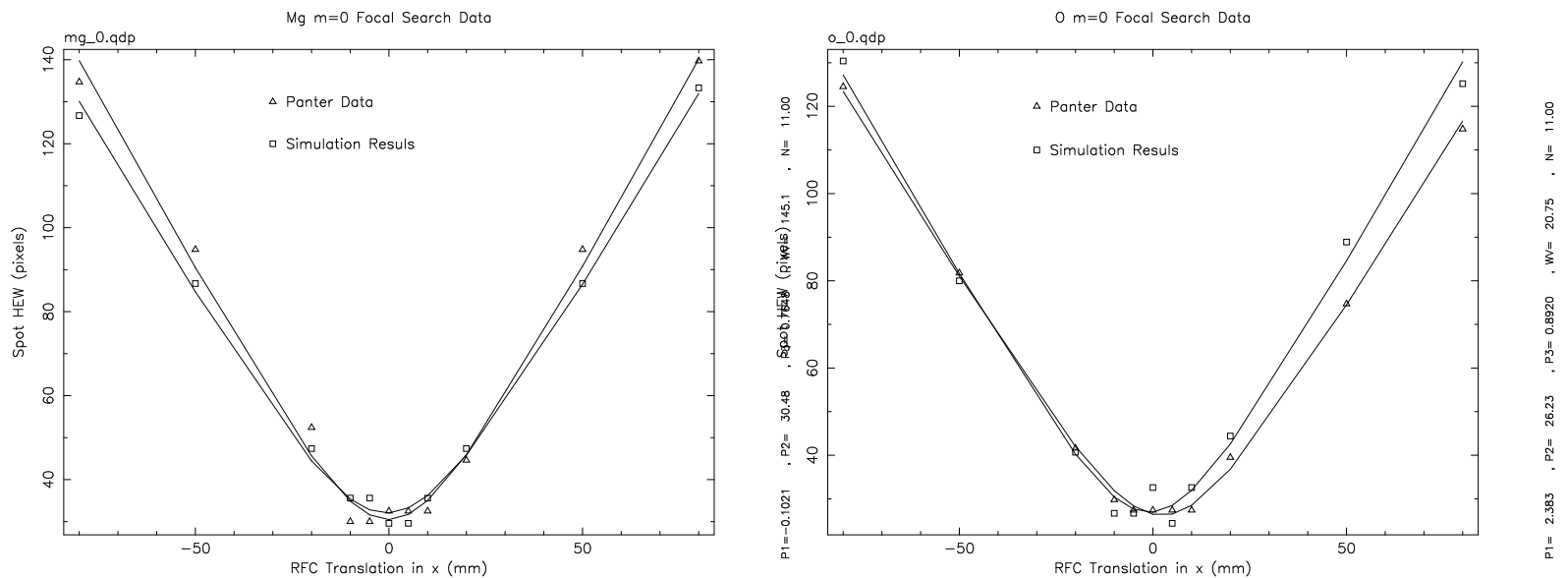


Figure 24: Sample focus searches from RGS1/RGA2. Only spot widths in the dispersion direction are shown. Panter data and simulated data are overlaid in each plot.

4.2.2 Gluecksrad results

The reader is referred to section 2.2 for sample plots of gluecksrad profile comparisons as well as the map of gluecksrad aperture positions. In the interest of brevity, those are the only such plots included in this document.

Figure 25 shows a plot of spot centers for the full set of RGS1/RGA2 gluecksrad measurements from the April 1998 Panter run. Figure 26 displays the same data in four separate plots, separated by gluecksrad angular sector. The horizontal axes represent the angular position of the gluecksrad aperture illuminating the CCD. The vertical axes represent the linear offset on the CCD of the spot center.

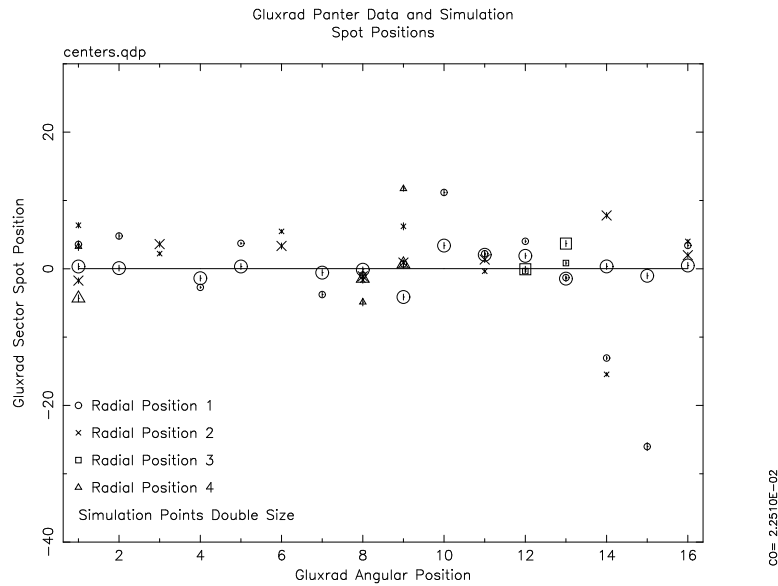


Figure 25: Plot of all gluecksrad spot centers. The horizontal axis shows the sector number, which is proportional to ϕ_{RGA} , the polar angle around the RGA. The vertical axis shows the linear offset of the spot center with respect to the overall average. This plot may be compared with figure 14, which exhibits a cosinusoidal trend not present here. Large markers represent centers of simulated data, small markers represent centers of real data.

As compared with the results presented in section 4.1, the present results show no cosinusoidal trend in positions of spot centers with angular position of gluecksrad aperture. This consistency results from having corrected for the interferometer malfunction prior to assembly of RGS1/RGA2, which was built after the testing of RGS2/RGA1.

As with the gratings in gluecksrad sector 8,4 in RGS2/RGA1, the gratings in gluecksrad sectors 14,1; 14,2; and 15,1 appear as outliers. The gluecksrad profiles of sectors 14,1 and 14,2 also show no increased dispersion and the shapes of the simulated peaks nearly replicate those of the real data. These results imply a coherent misalignment, as with sector 8,4 above. Sector 15,1 shows some broadening, as with sector 10,1 in RGS2/RGA1, but to a smaller extent, which may suggest some grating twist. Either the twist was erroneously not observed during assembly or it was introduced during environmental testing.

To resolve this issue, the gratings in this sector were observed visually for signs of movement arising from environmental testing, with no conclusive findings. Again, since no existing measurement has resolved the nature of the misalignments, and since environmental testing appears to have been ruled out as a cause (somewhat inconclusively in the case of sector 15,1), the few percent of the X-rays incident on these gratings will likely remain as modeled here.

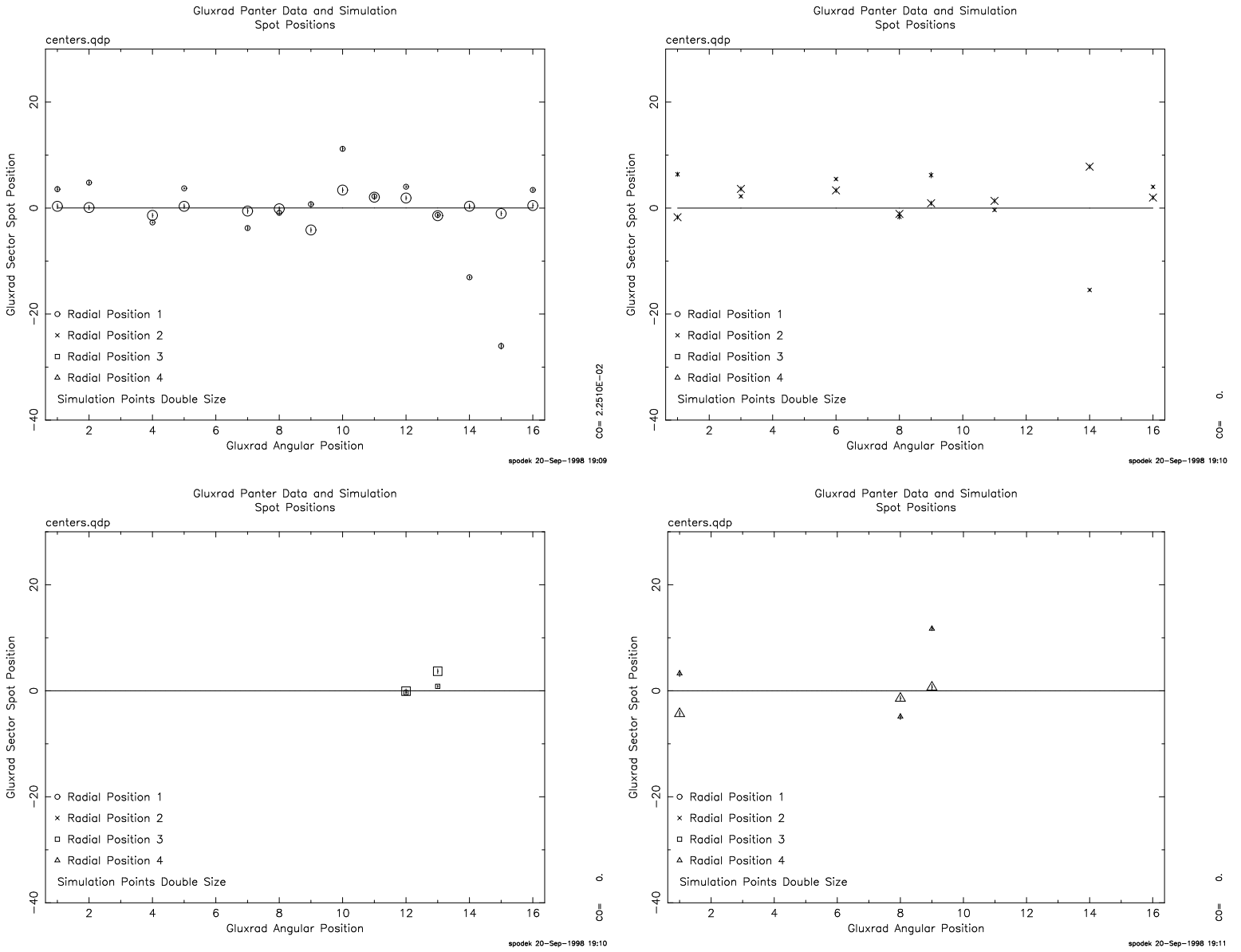


Figure 26: Same as previous figure, but separated by the four gluecksrads angular sectors.

4.2.3 Gluecksrad composites

Figures 27–28 show the gluecksrad residuals between real data spot positions and simulated spot positions. Again, no obvious trends are apparent. Figure 29 shows a histogram of the residuals in figures 27–28. The standard deviation of its distribution is approximately the same (a few percent lower) as the same distribution in RGS2/RGA1 after corrections for the interferometer error.

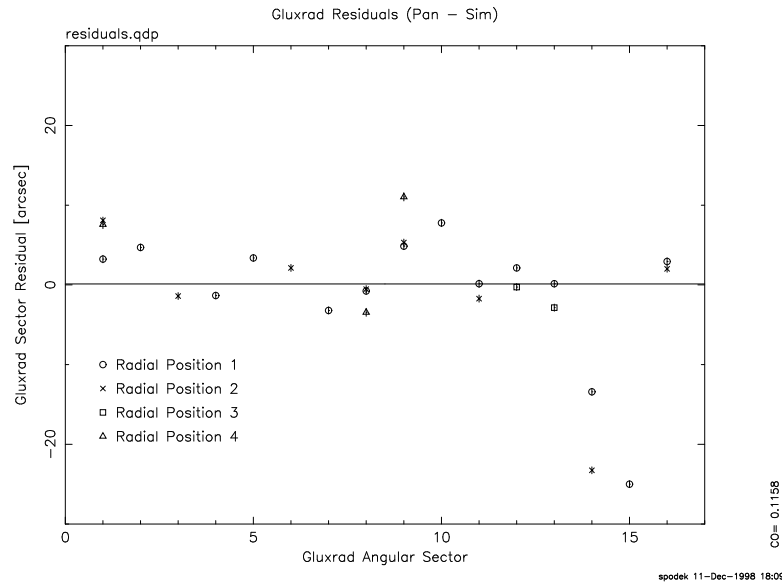
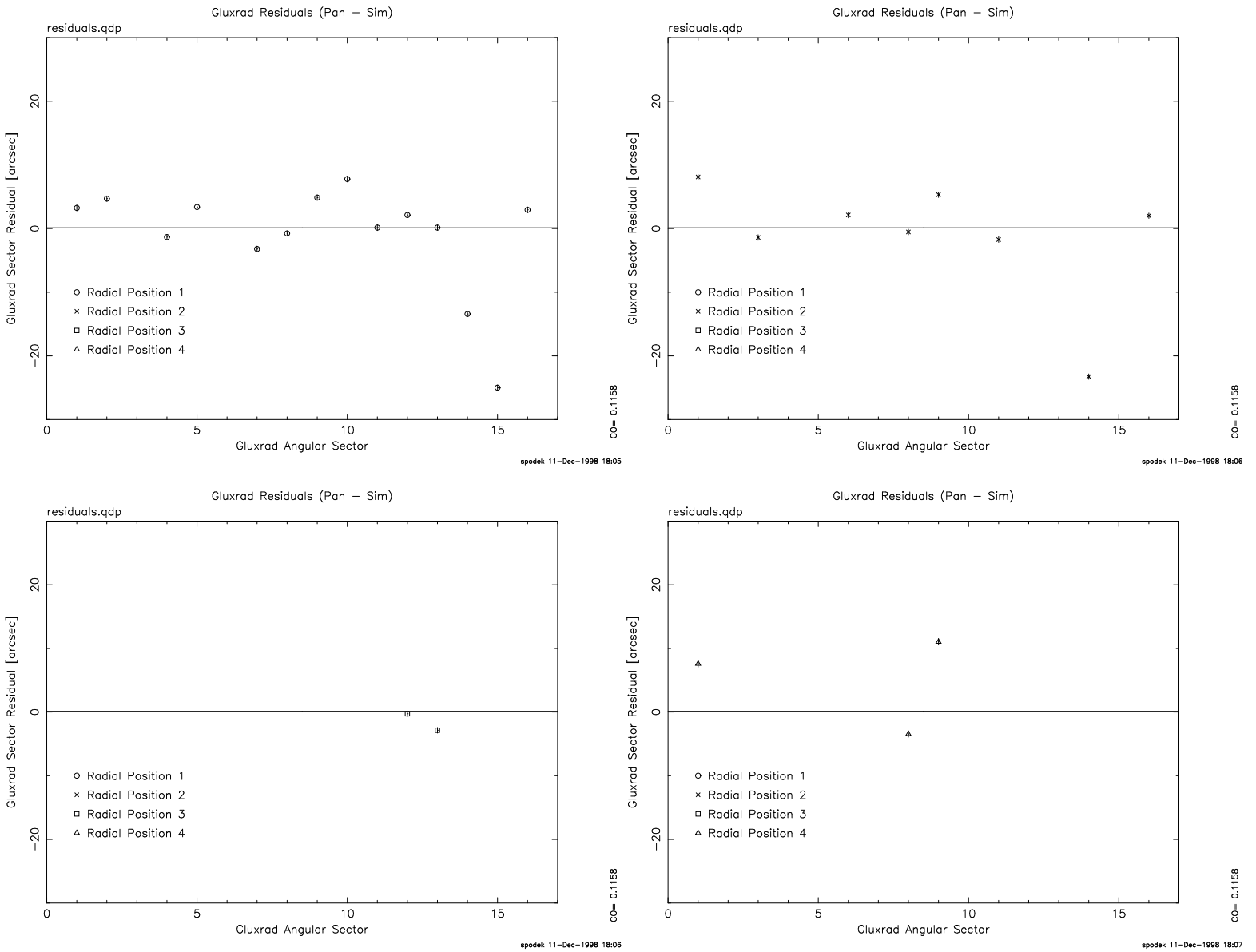


Figure 27: Plot of all gluecksrad spot center residuals. The axes are the same as the previous plots.

As a further check against trends in CCD spot position with grating position on the RGA, figure 30 displays the spot position on the CCD as a function of the linear position on the RGA of the open gluecksrad aperture. A trend like that seen in RGS2/RGA1 would appear as a straight line in this plot. No such trend is apparent.



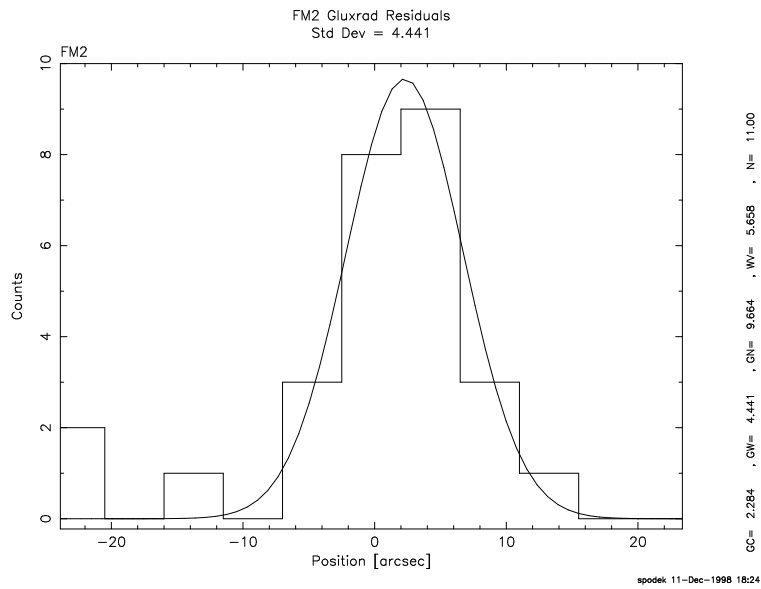


Figure 29: Histogram of the residuals in the previous figures with a Gaussian overlaid.

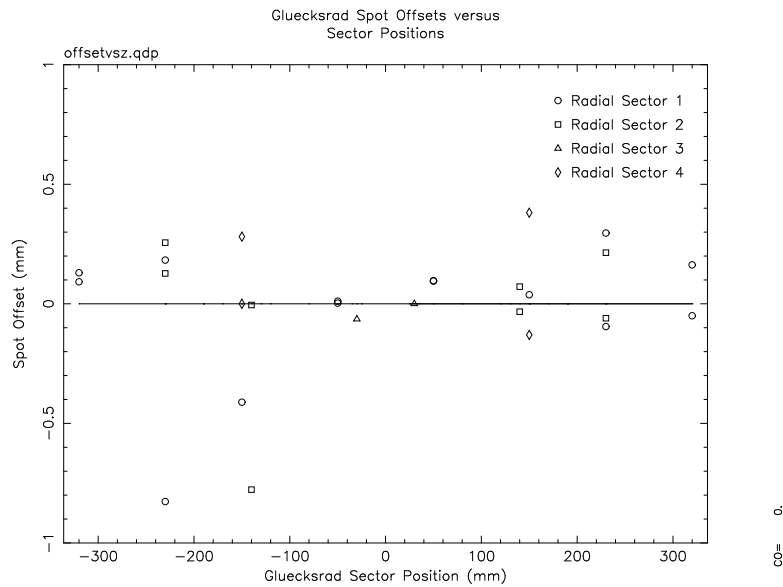


Figure 30: Plot of the spot position on the CCD as a function of z , the linear position on the RGA of the open gluecksrad aperture.

4.2.4 Full box results

As noted in section 2.3, the criteria for choice of diagnostic line—high energy, narrow lines, high order, and high scatter—as well as the logarithmic vertical axes all conspire to make the full box profiles look worse. The reader is reminded when looking at an apparently broad line that this appearance is either superficial or a sign of the line's diagnostic power.

Also as noted in section 2.3, the χ^2 values quoted for each plot do not refer to a fitting that allowed a change in profile shape, only recentering and renormalizing the simulated data relative to the real data. Variation of these parameters does not affect the shape of the profile.

All plots are shown with the same horizontal scale. Vertical scales are consistent within lines of the same source, but vary from source to source. All fitting is performed over the horizontal range plotted with three exceptions. For Al K, $m=-3$, $-2 < \Delta z < +2$ was the fitting region, due to a low signal to noise ratio outside that region. In the cases of Si K, $m=-2,-3$, the fitting did not converge so the plots shown are not fitted, simply overlaid, and the reported χ^2 is meaningless.

Binning is performed to a minimum of ten counts per bin for proper χ^2 statistics. All simulation hardware positions are according to Panter encoder measurements, sometimes adjusted for greater accuracy if possible through Tamsop.

The following full box results are presented for RGS1/RGA2:

1. RGS1/RGA2 Al, $m=0,\dots,-3$
2. RGS1/RGA2 Mg, $m=0,\dots,-3$
3. RGS1/RGA2 O, $m=0,\dots,-2$
4. RGS1/RGA2 Si, $m=0,\dots,-3$

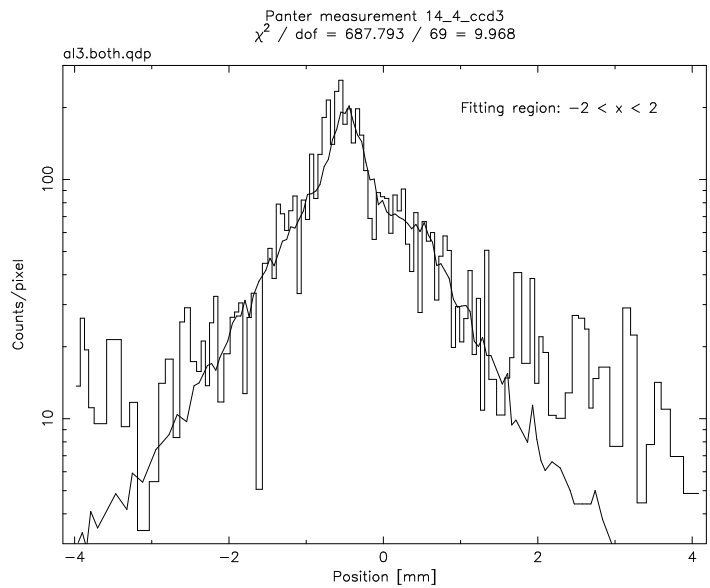
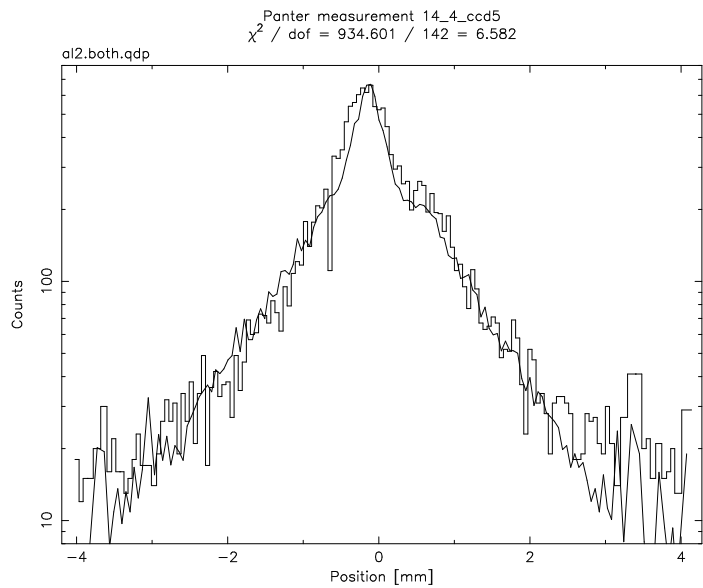
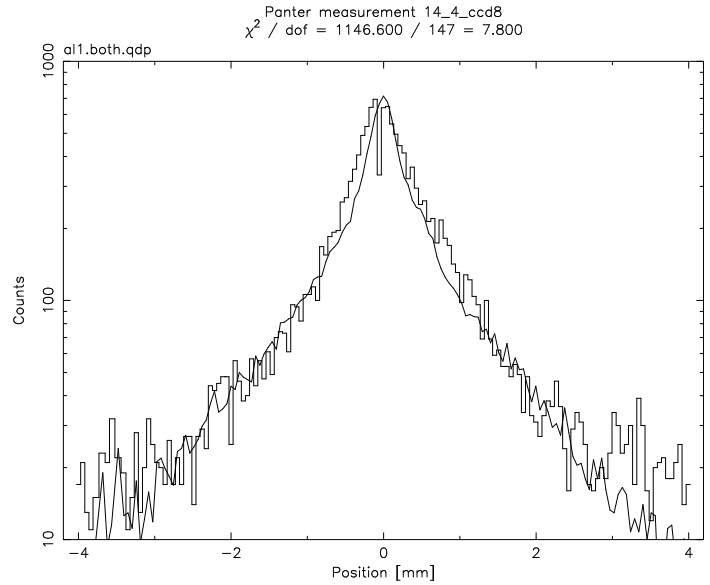
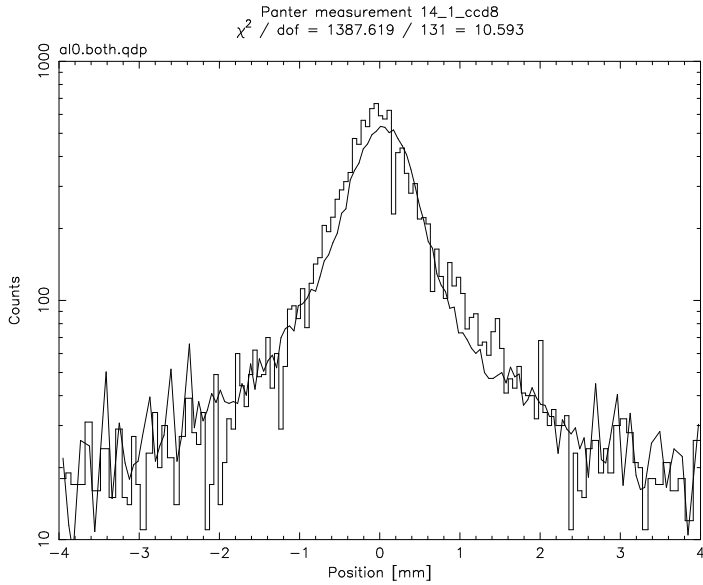


Figure 31: Plots of the full box Al K data from RGS1/RGA2. In the highest order profiles, where the fraction of scattered light is large ($>50\%$), first order scattering theory breaks down in predictions of both scattering fraction and profile shape. The consistency between data and model is about as good as can be expected.

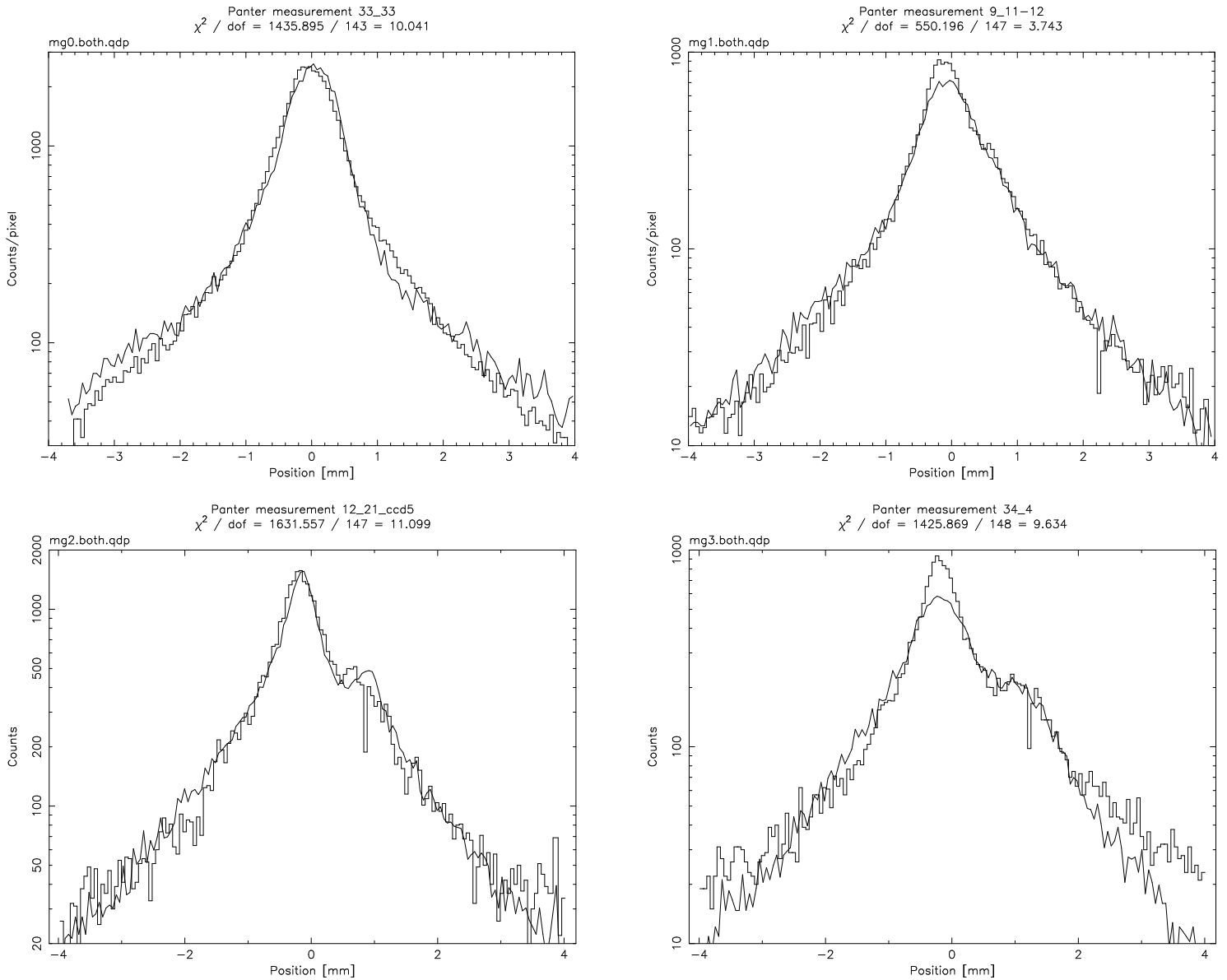


Figure 32: Plots of the full box Mg K data from RGS1/RGA2. In the highest order profiles, where the fraction of scattered light is large (>50%), first order scattering theory breaks down in predictions of both scattering fraction and profile shape. The consistency between data and model is about as good as can be expected.

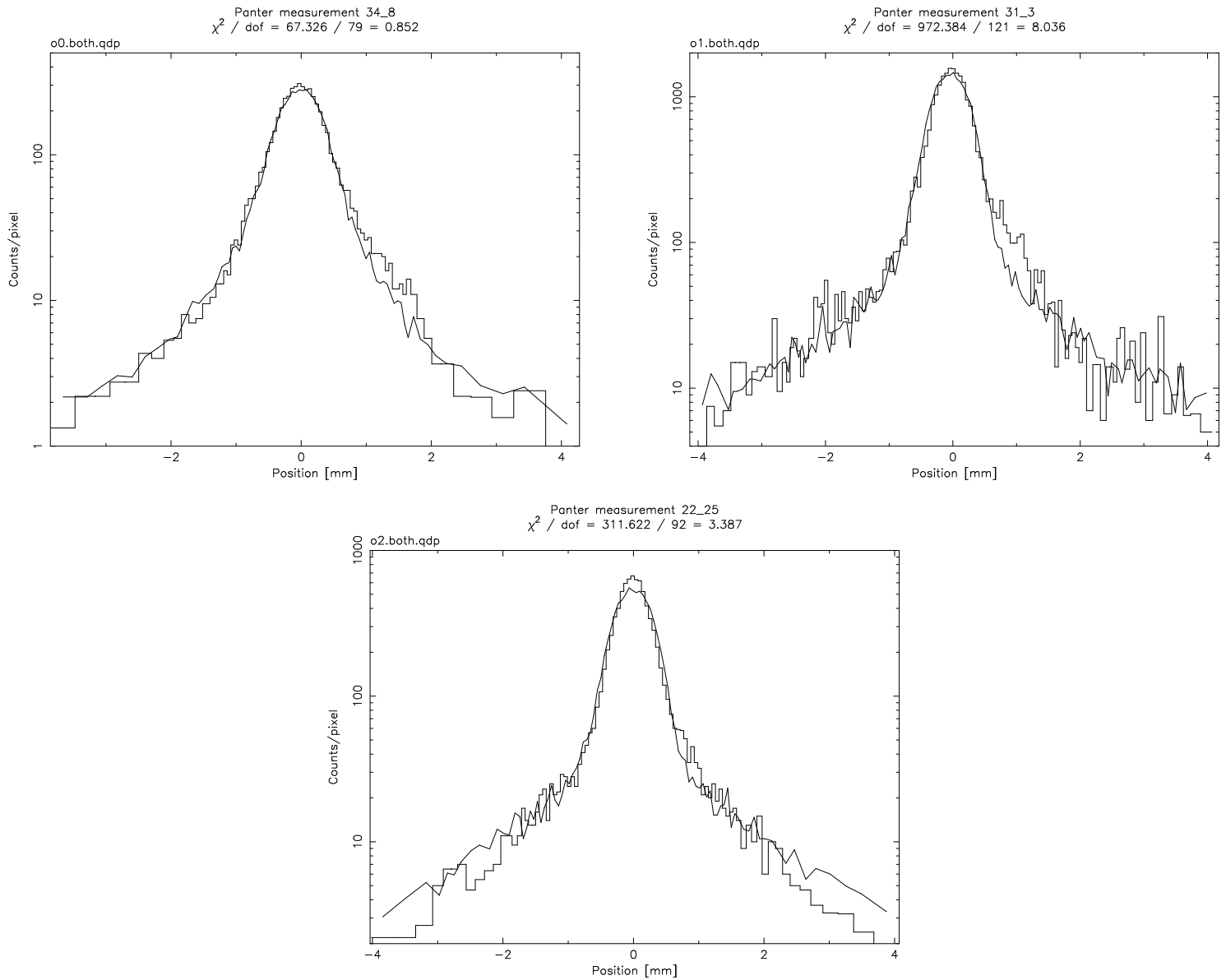


Figure 33: Plots of the full box O K data from RGS1/RGA2

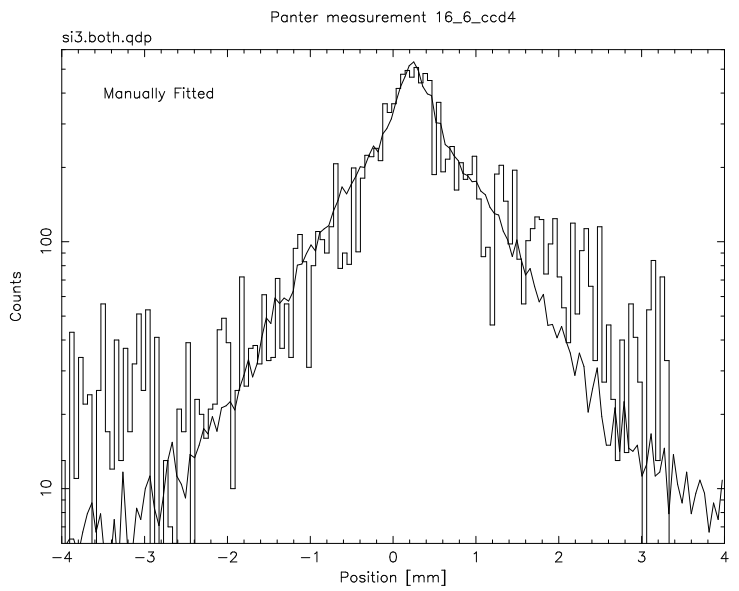
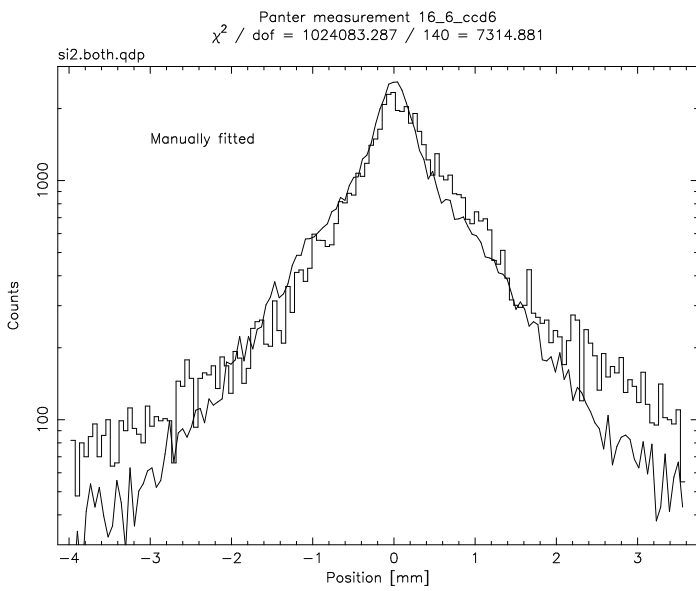
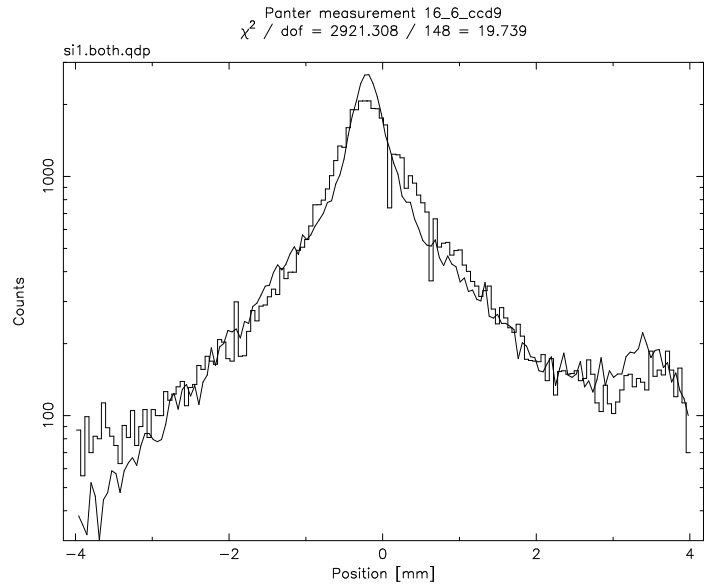
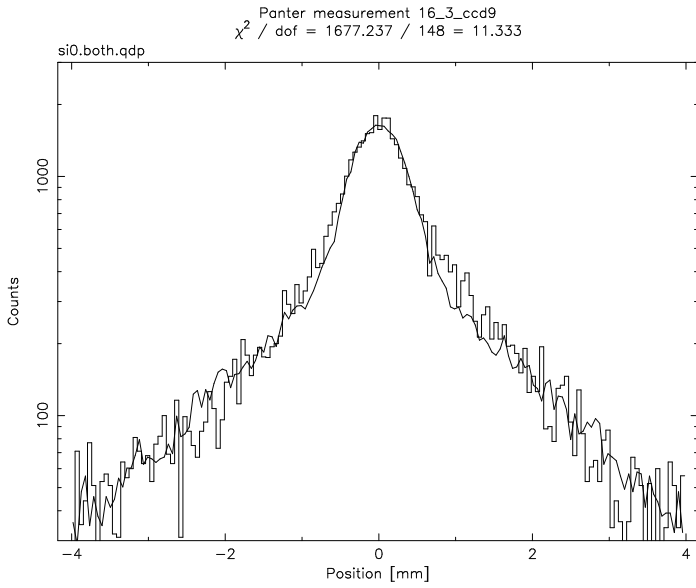


Figure 34: Plots of the full box Si K data from RGS1/RGA2

Columbia Astrophysics Laboratory	XMM-RGS	Doc.: RGS-COL-CAL-98027 Page: 52 Auth.: Joshua Spodek Date: December 21, 1998
---	----------------	--

References

- [1] Citrin, P., et al *Linewidths in X-ray photoemission and x-ray emission spectroscopies*; Phys Rev B, August 15, 1974
- [2] Erd, C. and Spodek, J. *Scisim / Columbia Raytrace Benchmark Test Suite*;
<http://astro1.nevis.columbia.edu>, December 10, 1998
- [3] Paerels, F., et al. *Modeling and Analysis of X-ray Emission Line Images Acquired with a Prototype Model of the Reflection Grating Spectrometer*; Proc. SPIE, July 29, 1994
- [4] Brinkman, A.C., et al. *Preliminary Test Results on Spectral Resolution of the Low Energy Transmission Grating Spectrometer on board of AXAF*; Proc SPIE, 1997
- [5] den Herder, J.W. *Panther RGS: alignment results RGS1 configuration C, A summary report*; SRON document, Dec. 8, 1997
- [6] Cottam, J. *TAMSOP Analysis of Panther Alignment*;
<http://astro1.nevis.columbia.edu/xmm/documents>, Feb. 1, 1997
- [7] Spodek, J. *Measurement of Single Grating Scatter at the Nevis Longbeam Facility*;
<http://astro1.nevis.columbia.edu/xmm/documents>, Feb. 1, 1997
- [8] Paerels, F. *Preliminary Analysis of the FM1/B0 Point Spread Function Data Acquired During FM1/Panther2*; <http://astro1.nevis.columbia.edu/xmm/documents>, December 7, 1997
- [9] Spodek, J. *Reanalysis of Panther FM1 LSF Data*; <http://astro1.nevis.columbia.edu>, October 31, 1997
- [10] Rasmussen, A. *The Initial Grating Misalignment Distribution for RGA/FM1*;
<http://astro1.nevis.columbia.edu/xmm/documents>, September 28, 1997
- [11] Paerels, F. *Repositioning the RGA and RFC on FM1*;
<http://astro1.nevis.columbia.edu/xmm/documents>, March 8, 1997
- [12] Rasmussen, A. *Internally Consistent Determination of the Optimal Rowland Circle for RGA/FM2*;
<http://astro1.nevis.columbia.edu/xmm/documents>, May, 3, 1998
- [13] Paerels, F. *The Intrinsic Focal Length of RGA/FM2 is 6700.00 mm*;
<http://astro1.nevis.columbia.edu/xmm/documents>, May 25, 1998
- [14] Rasmussen, A. *Initial Grating Misalignment Distribution for RGA/FM1, II*;
<http://astro1.nevis.columbia.edu>, October 14, 1997

Columbia Astrophysics Laboratory	XMM-RGS	Doc.: RGS-COL-CAL-98027 Page: 53 Auth.: Joshua Spodek Date: December 21, 1998
---	----------------	--

Contents

1	Introduction	1
2	List of Panter Measurements	2
2.1	Focal Searches	2
2.2	Gluecksrad	3
2.3	Full Box	7
2.4	Detailed list of Measurements performed	8
3	Description of the Physical Model: What we know and how we know it	12
3.1	Line Profiles	12
3.1.1	General	13
3.1.2	Core Wavelengths	13
3.1.3	Core Widths	13
3.1.4	Satellite separations and relative intensities	13
3.2	Telescope Model	14
3.3	Measurement Geometry	16
3.3.1	Apparatus position uncertainties	16
3.3.2	Apparatus positioning reproducibility	16
3.3.3	Spot position predictability	17
3.4	Mechanical Tolerancing on Grating Positions	18
3.4.1	Assembly room data: individual grating misalignments and bow	18
3.4.2	Machining Specifications	21
3.5	Scattering Model	22
4	Review of measurement results	26

4.1	RGS2/RGA1	26
4.1.1	Focal searches	26
4.1.2	Gluecksrad results	29
4.1.3	The problem with RGA1	31
4.1.4	Gluecksrad composites	33
4.1.5	Full box results	35
4.2	RGS1/RGA2	40
4.2.1	Focal searches	40
4.2.2	Gluecksrad results	41
4.2.3	Gluecksrad composites	44
4.2.4	Full box results	47